Materials Science & Engineering A 862 (2023) 144411

Contents lists available at ScienceDirect

Materials Science & Engineering A

journal homepage: www.elsevier.com/locate/msea

Experimental characterization of voids and surrounding microstructures developed under tension of Mg, Mg–3Zn, and Ti: A statistical study

Evgenii Vasilev, Marko Knezevic *

Department of Mechanical Engineering, University of New Hampshire, Durham, NH, 03824, USA

ARTICLE INFO

Keywords:
Microstructures
Twinning
Grain fragmentation
Voids
Magnesium
Titanium

ABSTRACT

This paper presents the main findings acquired in an experimental investigation into where voids form in microstructures of pure Mg, Mg–3Zn alloy, and pure Ti after tension to near fracture. To facilitate a statistical study, 52 voids in Mg and 62 voids in Ti along with local microstructures surrounding them were observed using a high-resolution electron backscattered diffraction (EBSD) mapping. Distributions capturing shape and orientation of voids with respect to loading direction were created as these geometric features give rise to local stress concentrations. Microstructural evolution and, in particular, the formation of deformation twins as local heterogeneities in the structures was observed to significantly influence the formation of voids in both Mg and Ti since these metals accommodate plastic strains by profuse twinning and grain fragmentations in addition to slip. To this end, distributions featuring the number of twin families neighboring each void, specific twin family neighboring each void, and voids taking shape of prior twins were formed. The observations and distributions reveal that formation of voids is driven by local microstructural heterogeneities, which are predominantly twins for Mg and predominantly grain fragmentations including shear bands for Ti. While substantial number of voids neighbor at least one twin family in both Mg and Ti, voids are predominantly twin-like i.e., lamellar in Mg but predominantly spherical in Ti. While the lamellar voids in Mg are elongated in the direction of twins, which is typically greater than $\pm 30^{\circ}$ from a pulling direction, a minor content of elongated voids in Ti align with the pulling direction. Such statistical distributions along with qualitative observations are presented and discusses highlighting the comparisons between the two metals exhibiting substantial differences in ductility and fracture behavior.

1. Introduction

Understanding and predicting fracture is fundamental to the design and adoption of improved and new structural materials with enhanced strength, ductility, and toughness. Strong yet sufficiently ductile materials are of special importance in engineering design to avoid rapid brittle fracture of critical structures [1–3]. Ductile fracture typically happens by nucleation, growth, and coalescence of voids [4–7]. It is well established that voids can be induced by plastic deformation, especially in microstructural regions of intense localized deformation [8–13]. Previous research has shown that microstructural features such as grain boundaries [8,14–16], phase boundaries [17–20], twin-parent boundaries [14,21–23], inclusions/precipitates [13,24–29], hydrides [30], vacancies [31,32], softening due to local recrystallization [11,33], and dislocation interaction heterogeneities [34–37] can act as initial void nucleation sites. While twins provide an additional degree of freedom to facilitate plasticity [38–44], they introduce heterogeneities in the microstructure and therefore influence the formation of voids [45,46]. To formulate microstructure-based models for predicting fracture, it is of special importance to know on which microstructural feature voids preferentially nucleate during plastic deformation of ductile metals. Knowing such weak links in structures and having the models can enable creation of metals more resistant to fracture.

From the perspective of fracture mechanics, it is essential to determine shape and orientation of discontinuities in the microstructure [47,48] as these govern mechanical fields responsible for crack propagation behavior and ultimate fracture [5,49]. Elongated defects present much higher stress concentrations then spherical ones [50–52]. For example, value of the stress concentration factor determined from Ingles equation [53] will be almost 4 times higher for an elongated defect with an ellipse

* Corresponding author. University of New Hampshire, Department of Mechanical Engineering, 33 Academic Way, Kingsbury Hall, W119, Durham, NH 03824, United States.
E-mail address: marko.knezevic@unh.edu (M. Knezevic).

https://doi.org/10.1016/j.msea.2022.144411
Received 25 August 2022; Received in revised form 23 November 2022; Accepted 24 November 2022
Available online 29 November 2022

ratio of 5 compared to a circular defect with an ellipse ratio of unity. The effect of void orientation on stress concentrations can be estimated from the equations of the stress intensity factors [5]. An angle between the loading axis and the long axis of the defect is a variable in those equations.

Attempts to link the local microstructure and void nucleation are not new though studies are typically performed on datasets of a few observations [10,21,54,55]. However, the observed local phenomena do not always represent a homogenized behavior of the material. Therefore, statistical studies are needed to establish more reliable correlations since fracture should be studied in a statistical and not in a deterministic way [56–60]. Lack of statistical studies such as [17,61,62] is explained by complexity and time demands of the required experimental techniques [63–65]. In an attempt to alleviate this problem, in this work we present findings derived from a comprehensive dataset of microstructural data acquired around 114 voids in Mg and Ti. With numerous observations of different voids in Mg and Ti, we provide statistical information on void characteristics as well as correlation between location of voids and local microstructures.

Mg and Ti and their alloys are metals, which have many desirable intrinsic properties (e.g. lightweight, biocompatible) [66–75]. In particular, these metals are receiving increasing interest for structural components, because of their high strength-to-weight ratio. While both are anisotropic, they exhibit substantial differences in ductility and fracture behavior. The particular samples for the study, pure Mg, Mg–3Zn alloy, and pure Ti, are treated to have coarse-grained initial microstructures to magnify the grain-scale phenomena taking place during deformation and fracture [76–79]. The samples are pulled in tension to near fracture, then voids are confirmed using X-ray tomography, and finally characterized using electron back-scattered diffraction (EBSD). Results of the characterization are presented qualitatively and in the form of statistical distributions. Insights from these are described and discussed in the paper.

2. Materials and experimental procedures

In this work, three different materials are used: Ti with nominal purity 99.999%, Mg with nominal purity 99.99%, and a Mg-3 wt.%Zn alloy. These materials will be referred later in the text as pure Ti, pure Mg, and Mg–3Zn, respectively. Pure Mg and pure Ti have no second phase particles that can act as a void nucleation sites [14,25]. Therefore, the complexity of the analysis of these two pure metals renders to heterogeneities such as grain boundaries, grain fragmentation, twins, and shear bands. Similarly, with light alloying of Mg with 3 wt% of Zn and following annealing with relatively fast cooling, the alloy forms supersaturated solid solution of Zn in Mg with minimal presence of very fine precipitates that are unlikely to serve as void nucleation sites in contrast to coarse coagulated particles.

Pure Ti was rolled into a 10 mm thick plate and annealed at 800 °C for 24 h. Pure Mg was also rolled in a 10 mm thick plate and annealed at 450 °C for 24 h, while the Mg–3Zn alloy was extruded at 350 °C with an extrusion ratio 9:1 and annealed at 413 °C for 24 h. All anneals were done in an argon atmosphere. Samples of pure Mg and pure Ti were cooled in the furnace with flowing argon. Samples of Mg–3Zn were air cooled to minimize nucleation of coarse precipitates of the MgZn second phase. The idea behind the designed heat treatments was to grow grains to magnify microstructural phenomena occurring during plastic deformation [76–78]. With larger grains, we expect nucleation of larger voids that are easier to capture by standard experimental techniques such as X-ray tomography and SEM/EBSD.

The annealed materials were cut into 2 mm thin plates by spark erosion and milled or spark cut into tensile specimens. Geometry of the specimens is presented in the appendix. Mechanical testing was performed using a Gatan microstage with max load of 2 kN. Tension was performed along the rolling direction (RD) of the rolled sheets and the extrusion direction (ED) of the extruded rods. Tension tests were interrupted at strain levels with anticipated formation of voids. X-ray tomography imaging followed to confirm presence of voids. Verification by tomography was necessary for samples of pure Ti in particular

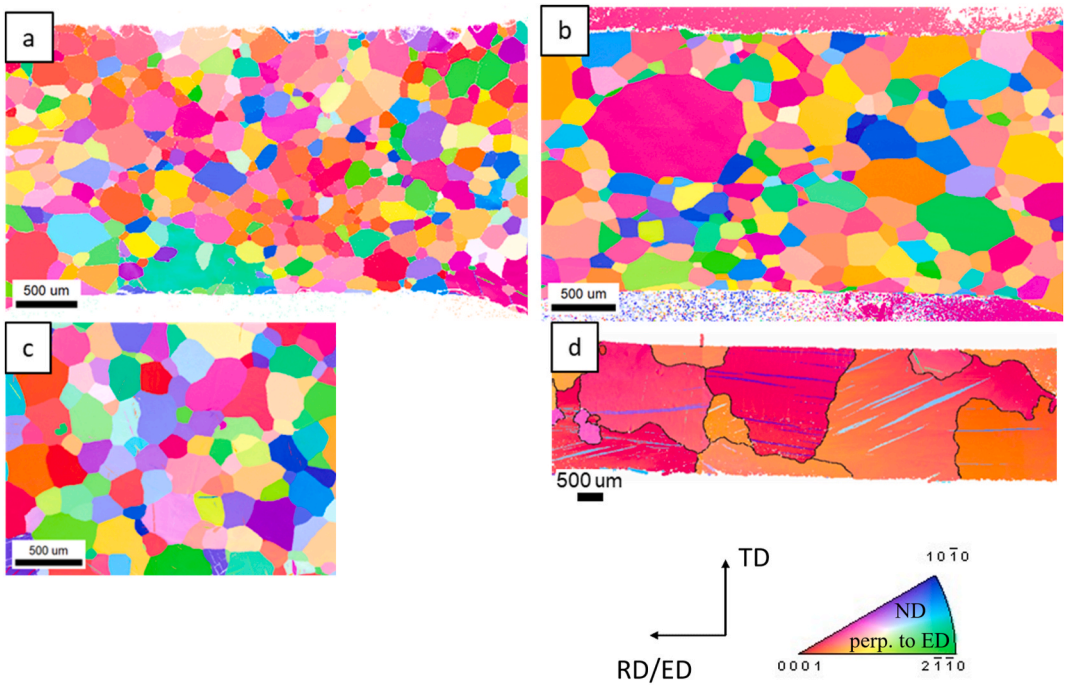

Fig. 1. (a–d) IPF maps showing the initial microstructure in the tensile specimens of (a,b) pure Ti, (c) Mg–3Zn, and (d) pure Mg. (a–d). The maps correspond to samples 1, 2, 4, and 7 in Fig. 2, respectively. The sample direction perpendicular to the maps is ND or perpendicular to ED as indicated in the standard IPF triangle. The colors in the IPF maps represent the orientation of ND/PED sample axes with respect to crystal lattice frames according to the coloring in the standard IPF triangle. (For interpretation of the references to color in this figure legend, the reader is referred to the Web version of this article.)

because these samples exhibited prolongated deformation and pronounced necking. Samples of pure Mg and Mg–3Zn alloy fractured right after reaching ultimate tensile strength (UTS), so samples of these materials were tested approximately to right after UTS. Nevertheless, some of the Mg samples fractured during testing. Voids were observed near fracture surfaces for these samples. The exact numbers of samples that were pulled to near fracture and to fracture and characterized is eight, as will be described shortly.

X-ray computer tomography (μXCT) was performed on a Zeiss Xradia 610 Versa instrument under applied voltage of 40 kV and power at the tube of 1 W. The distance between source and the sample was 17 mm and the distance between 4x objective (detector) and the sample was also 17 mm, which resulted in the voxel size from 1.5 to 3 μm with binning 1 × 1 and 2 × 2, respectively. Scans were performed in 1601 projections per 360° and then reconstructed into 3D tomograms with drift correction using the Dragonfly software. If sufficient number of voids were present per tomogram (typically, a few tens of voids), the specimen was mount into a 1.25-inch polymer mount and polished for SEM/EBSD according to the procedure described below. If no voids were found or too few voids were observed, the tension test continued to create more voids or another sample was tested to near fracture.

For Ti, sample preparation for SEM/EBSD included the following: mechanical grinding on an abrasive paper of 320 grit, polishing using 9 μm diamond suspension, and final polishing using a mixture of 5 parts of colloidal silica and 1 part of H_2O_2. For Mg, the preparation included mechanical grinding on abrasive papers up to 2500 grit, polishing using 3 μm diamond suspension, and 1 μm diamond suspension, and final polishing using MasterPolish suspension (mixture of colloidal silica and alumina).

EBSD scans were performed at 10 kV with step size selected so every map contained about 600,000 points for undeformed samples and 200,000 points for deformed samples. EBSD data processing was performed in TSL OIM 8.6. Cleanup procedures included neighbor confidence index (CI) correlation, where points with CI less than 0.1 are replaced with neighboring points that have CI more than 0.1. Then, any remaining points with CI less than 0.1 were discarded from the dataset. EBSD scans were taken around 62 voids in Ti and 52 voids in Mg. The number of scans was sufficient to plot statistical correlations as analysis of the data casting about 75% of the data into the same statistical distributions as the full data did not change the trends. After EBSD scans were taken from the surface per specimen, polishing continued inside the specimens to observe more voids inside. Continued polishing was repeated usually five times. Example images along with identified voids at different depth in one of the samples are presented in the appendix. We would like to point out that acquisition of such a comprehensive experimental dataset of voids and surrounding microstructures was a significant challenge. Successful EBSD of heavily deformed Mg and Ti demanded preparation of many samples not all of which were successful and slow data acquisition speeds to achieve good quality of diffraction. Acquiring of over 100 scans took over 500 h of the SEM time, which was several months of data acquisition.

3. Results

This section begins by presenting the initial microstructures and flow stress response of the studied materials followed by a number of examples of qualitative observation, and finally presents a set of statistical distributions for properties of voids.

3.1. Initial microstructures and mechanical response in tension

Fig. 1 presents inverse pole figure (IPF) maps showing the initial microstructure in the tensile specimens of pure Ti (Fig. 1a and b), Mg–3Zn alloy (Fig. 1c), and pure Mg (Fig. 1d). Microstructures of two other pure Mg samples tested in this work are presented in Ref. [54]. The sample direction perpendicular to the maps is the normal direction (ND)

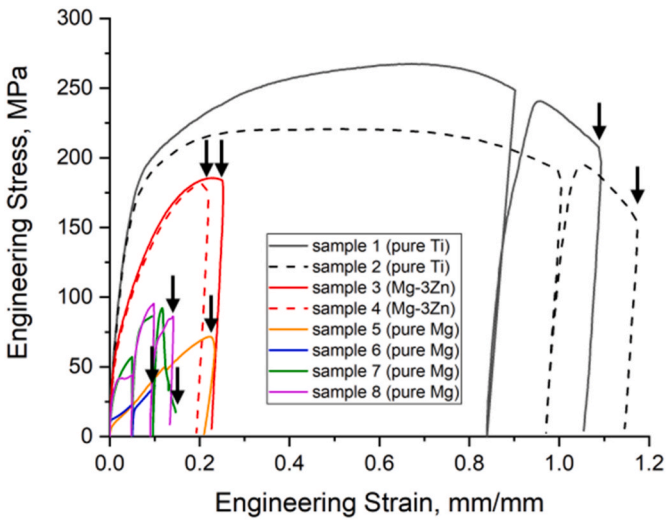

Fig. 2. Engineering stress-engineering strain curves measured for the specimens indicated in the legend in tension. Black arrows indicate strain levels at which EBSD scans were taken per specimen.

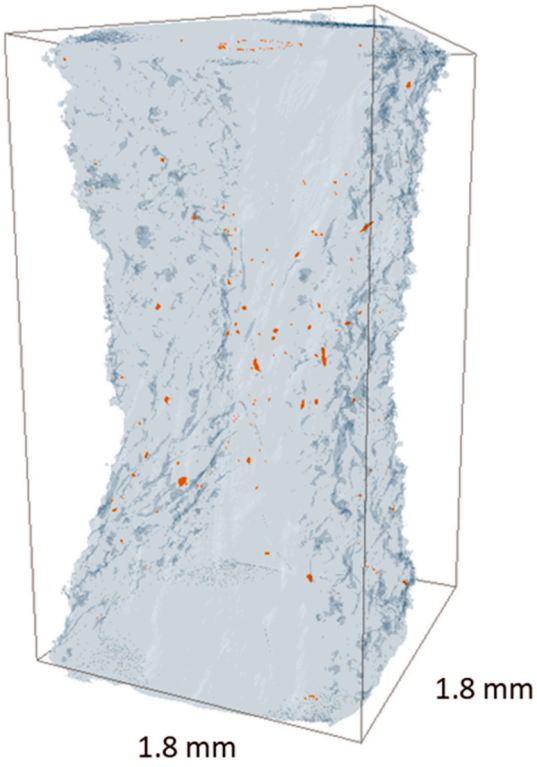

Fig. 3. X-ray tomogram of sample 1 necked region at an engineering strain of 1.1. In the tomogram, light blue color represents surface mesh, which is semi-transparent, while voids are highlighted with the opaque red color. (For interpretation of the references to color in this figure legend, the reader is referred to the Web version of this article.)

for the rolled sheets and perpendicular to the extrusion direction (PED) for the extruded rods as indicated in the standard IPF triangle. The colors in the IPF maps represent the orientation of the ND/PED sample axis with respect to the crystal lattice frame according to the coloring in the standard IPF triangle. Microstructures presented in Fig. 1a,b,c,d correspond to those of the stress-strain curves of the samples 1, 2, 4, and 7 in Fig. 2, respectively.

As we can see from these IPF maps, samples of pure Ti and Mg–3Zn

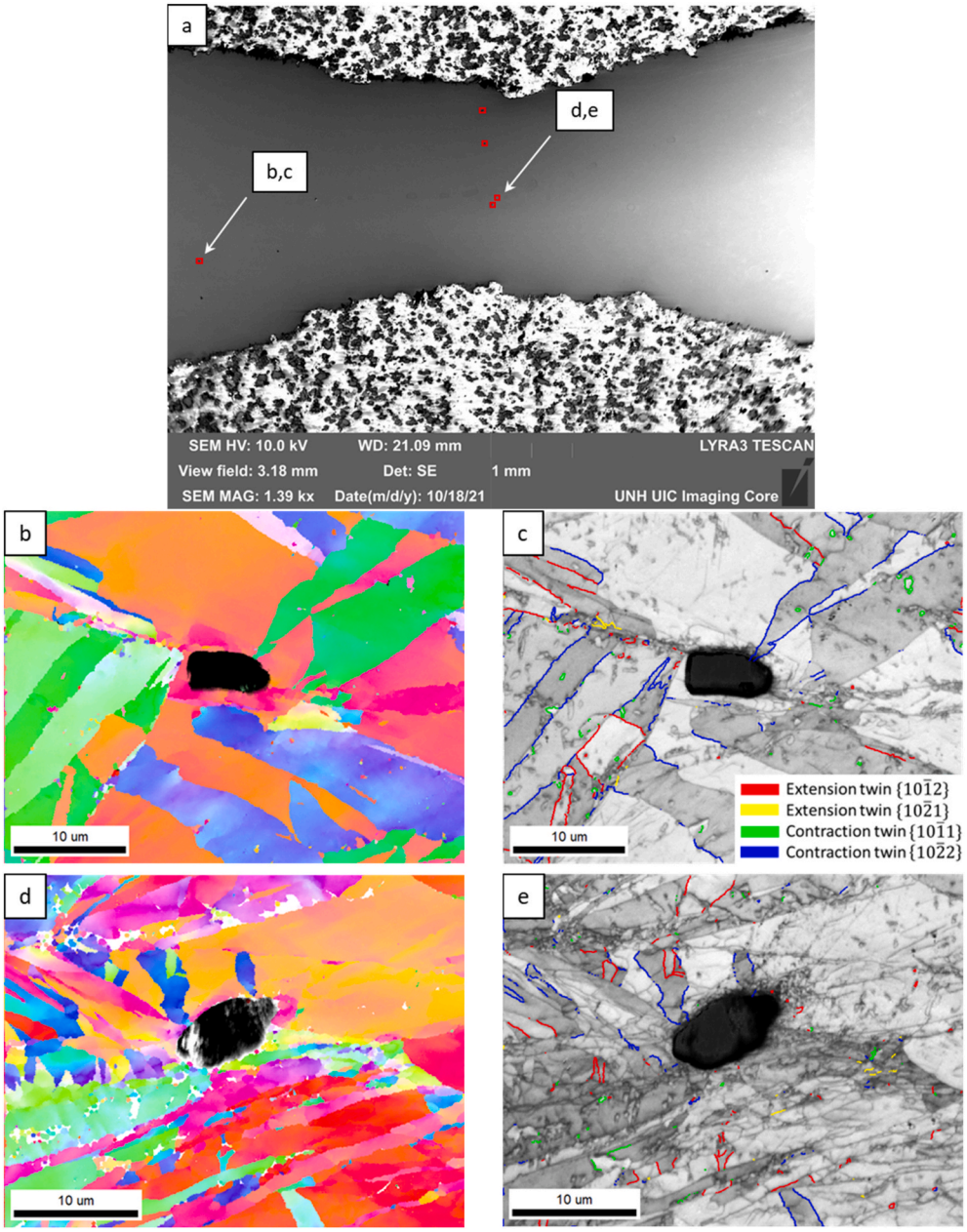

Fig. 4. (a) A secondary electrons (SE) SEM image of the gauge section after tension to an engineering strain of 1.1 of pure Ti (sample 1 after first polishing). Red squares in (a) highlight locations of pores. (b,d) IPF maps of the areas around pores indicated on (a) and (c,e) corresponding IQ maps with overlay of identified twin boundaries. Twin color code presented in (c) applies to all the following figures. (For interpretation of the references to color in this figure legend, the reader is referred to the Web version of this article.)

alloy have relatively homogeneous microstructures. The calculated grain size is 236, 368, and 265 μm for the samples in Fig. 1a, b, and c, respectively. Calculation of the grain size is not applicable for the sample presented in Fig. 1d as well as other pure Mg samples presented in Fig. 2 and in Ref. [54] because these are oligocrystalline specimens with grain size reaching a few mm.

Fig. 2 shows engineering stress versus engineering strain curves recorded for eight specimens tested in tension. Engineering and not true quantities are plotted to show post-necking portions of the curves. As it was described in the experimental section, tensile tests were interrupted at strain levels with anticipated formation of voids and followed by X-ray tomography to determine presence of voids. A typical tomogram with observed voids is presented in Fig. 3. If no voids to too few voids were present in a tomogram, the tensile test continued or a new specimen was tested. Specimens 1–5 were not pulled to fracture, while specimens 6–8 were pulled to fracture.

As evident from the stress-strain curves presented in Fig. 2, samples of pure Ti exhibited elongation of up to 105–115% with substantial reductions in their cross-sectional areas (Figs. 3a and 4a). The difference in the mechanical response between samples 1 and 2 is attributed to the differences in the initial microstructure as shown in Fig. 1. The lower strength specimen had slightly larger grain size (sample 2). Given that the tests were interrupted, elongation-to-fracture would even be higher for these specimens if deformed to fracture. Samples of the Mg–3Zn alloy exhibited much lower elongation at the observed void nucleation stage, on the order of 20%. Finally, the specimens of pure Mg showed significant differences in their mechanical response due to highly heterogeneous microstructures, which varied substantially from specimen to specimen [54]. Measured elongations ranged from 10 to 22%.

In this work, we do not attempt to establish correlations between the mechanical response and the initial and/or deformed microstructure as it lies beyond the research objective. The stress-strain curves are provided rather to illustrate at what strain (elongation) levels voids were observed and characterized in each material.

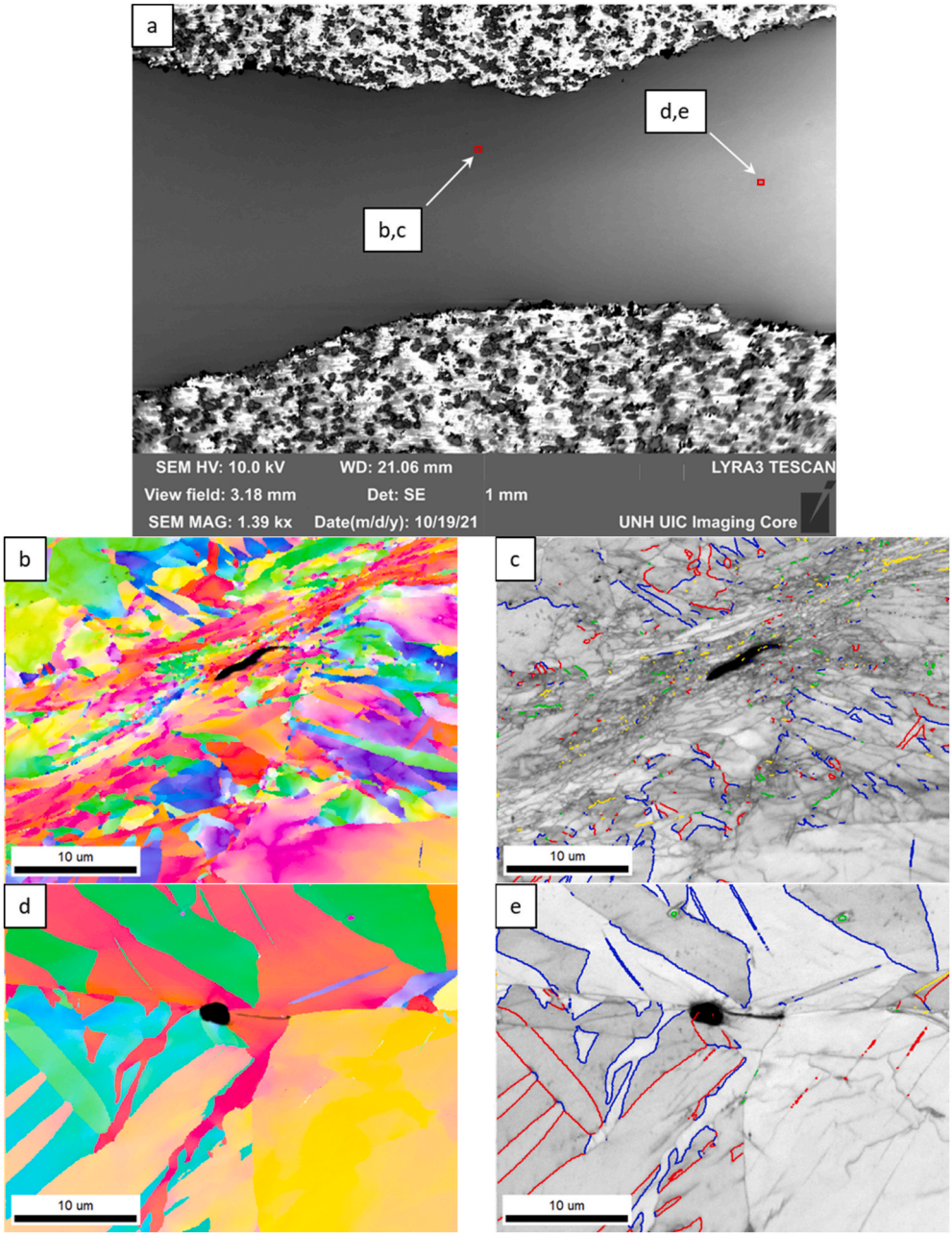

Fig. 5. (a) An SEM image of the gauge section after tension to an engineering strain of 1.1 of pure Ti (sample 1 after second polishing approximately 15 μm below the surface of Fig. 4a). Red squares highlight locations of pores. (b,d) IPF maps of the areas around pores indicated in (a) and (c,e) corresponding IQ maps with overlay of twin boundaries. (For interpretation of the references to color in this figure legend, the reader is referred to the Web version of this article.)

3.2. *Qualitative characterization of deformed microstructures*

After the tensile specimens were appropriately strained and voids confirmed, the samples were observed using SEM/EBSD. Figs. 4–7 illustrate first SEM images of gauge sections of tested samples of Ti (Figs. 4a and 5a) and Mg–3Zn (Figs. 6a and 7a). Red squares on the SEM images highlight locations of EBSD scans taken around voids.

Subsequently Figs. 4–7 show IPF maps (b,d) and corresponding image quality (IQ) maps (c,e) around pores that are indicated on the SEM images (Figs. 4a–7a). The IQ maps are plotted with an overlay of identified twin boundaries with color code presented in Fig. 4c. Note that the color code is applicable to all IQ + twin maps presented in the paper.

As evident from Figs. 4–7, deformed microstructures of both Ti and Mg become highly developed, fragmented and heterogeneous, with fragments to sub-μm scale. We do not provide quantification of grain size for deformed microstructures because large calculation errors would be inevitable. However, even qualitative judgement can highlight the significance of grain fragmentation. The fragmentation is dependent on twinning, which is clearly revealed in the IQ + Twin maps (Fig. 4c and e – Fig. 7c and e). From these figures, it is clear that almost all voids neighbor with twins and thus, twinning plays an important role in the formation of voids. This will be further considered in the statistical analyses that follows.

As far as spatial location of voids, it is evident that some voids nucleate on grain boundaries or junctions as in Fig. 4b and e, Fig. 5d and e, and Fig. 7d and e. In most cases, voids nucleate at multiple (>4) neighboring grains/fragments surrounded by numerous twins (Fig. 4d and e, Fig. 5b and c). Fig. 5 also illustrates an example of a void nucleated within a local shear band that is oriented ~45° to the loading

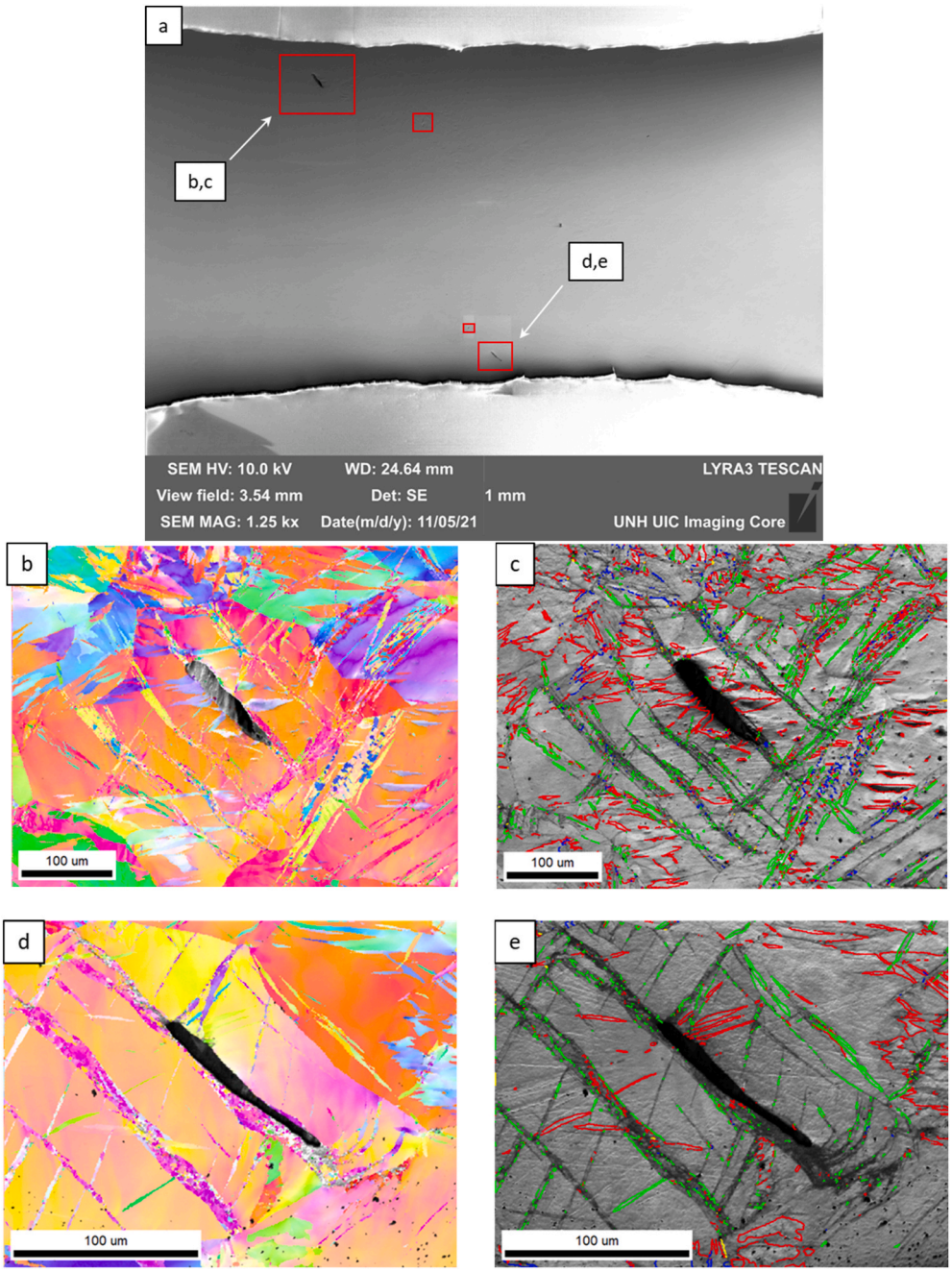

Fig. 6. (a) An SEM image of the gauge section after tension to an engineering strain = 0.24 of Mg–3Zn (sample 3 after initial polishing). Red squares highlight locations of pores. (b,d) IPF maps of the areas around pores indicated in (a) and (c,e) corresponding IQ maps with overlay of twin boundaries. (For interpretation of the references to color in this figure legend, the reader is referred to the Web version of this article.)

direction and contains highly fragmented microstructure. In such a case, the number of fragments neighboring the void is as high as 10–20 making establishing any reliable correlation between these fragments and the void difficult.

In summary, the qualitative observations show that voids in Mg and Ti have different, shape, size, and orientation with respect to the loading direction. Voids in Ti are more round (Fig. 4b–e, Fig. 5d and e) with a smaller number of elongated voids within shear bands (Fig. 5b and c). The size of these voids is typically within 10 μm. In contrast, in Mg, some ellipsoidal and many lamellar voids are observed that resemble shape of lenticular twins (Fig. 6b–e) and have size reaching 100 μm. Most of the voids in both Mg and Ti neighbor deformation twins.

To complement the above qualitative assessments, we performed analyses of Schmidt factors (SFs) for slip and kernel average misorientations (KAM) around voids. The SF analyses reveal the likelihood of basal ⟨a⟩slip {0001} as the easiest in Mg [80–85] and prismatic ⟨a⟩slip $\{\bar{1}100\}$ as the easiest in Ti [86–90] to operate around voids. The results are presented in Figs. 8 and 9. Fig. 8 shows color-coded SF maps for basal slip (a,c) and KAM (b,d) around voids in Mg, where (a,b) correspond to the location depicted in Fig. 6b and c, while (c,d) correspond to Fig. 6d and e. Fig. 9 displays color-coded SF maps for prismatic slip (a,d) and basal slip (b,e) as well as KAM maps (c,f) of areas around voids in Ti. Images shown in Fig. 9a, b and c and Fig. 9d, e and f correspond to the maps shown in Fig. 5b and c and Fig. 5d and e, respectively. The SF analyses reveal that lamellar-shaped voids in Mg are located on the boundary between prior contraction twins with high SF for basal slip and parent grains with low SF for basal slip. In contrast, no reliable

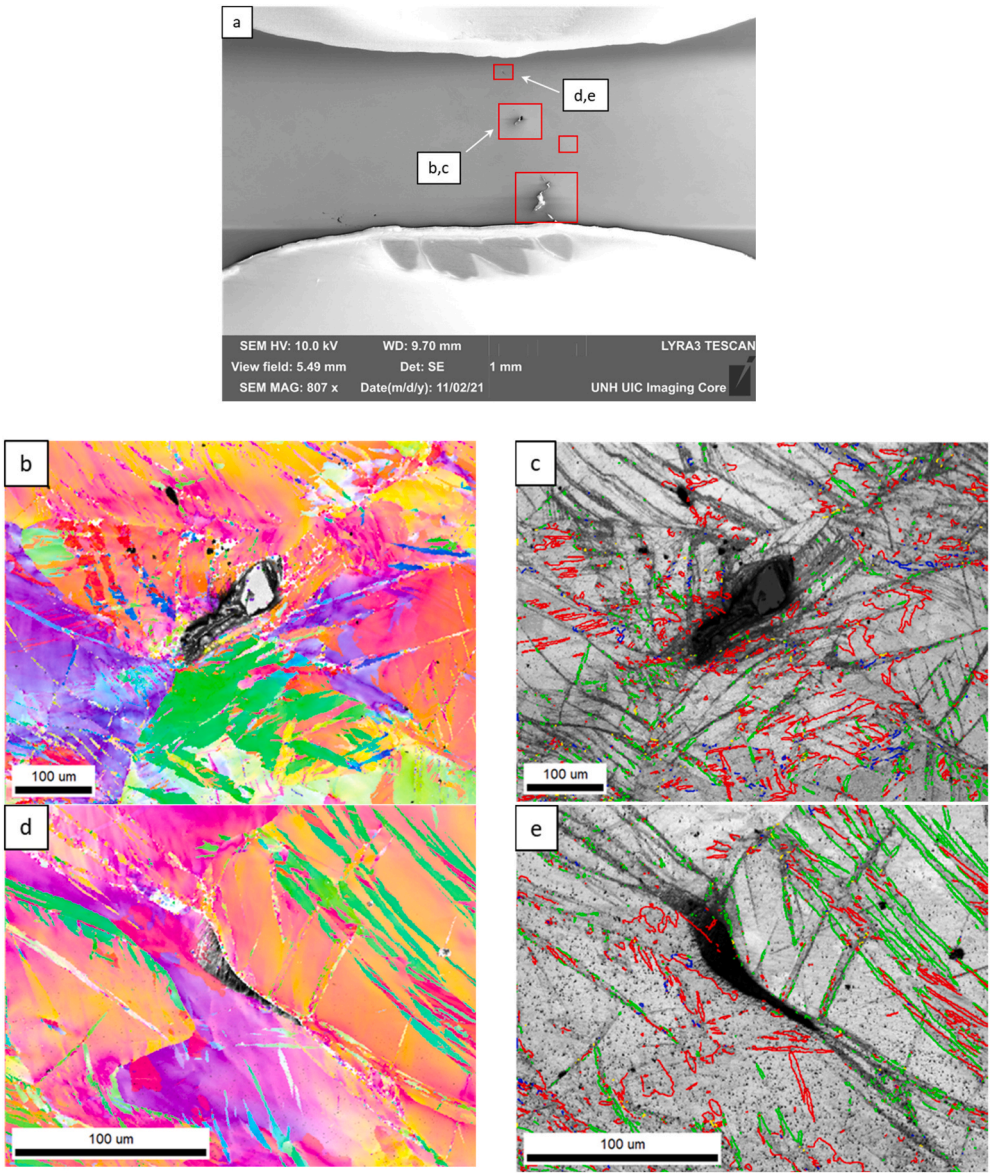

Fig. 7. (a) An SEM image of the gauge section after tension to an engineering strain of 0.21 of Mg–3Zn (sample 4 after initial polishing). Red squares highlight locations of pores. (b,d) IPF maps of the areas around pores indicated on (a) and (c,e) corresponding IQ maps with overlay of twin boundaries. (For interpretation of the references to color in this figure legend, the reader is referred to the Web version of this article.)

correlations can be established between location of voids and orientation of neighboring grains, SFs for basal or prismatic slip, and KAM in Ti, though voids are typically located in highly deformed regions. In the next section, we fit these qualitative observations into statistical distributions for further analyses.

3.3. Quantitative characterization of deformed microstructures

Given sufficient number of observations for each material (EBSD scans around 114 voids for Mg and Ti combined), the qualitative descriptions presented above are cast into statistical correlations. The following parameters are considered.

1. Void shape. Following the idea of increased stress concentrations with increasing ellipsoid factors and based on the observed void shapes in Fig. 4–7, this group is divided into several subcategories: (a) spherical voids with a ratio of long axis versus short axis of ellipsoid less than 2:1, (b) ellipsoidal voids with the ratio of long axis versus short axis of ellipsoid more than 2:1 but less that 5:1, (c) lamellar voids with the ratio of long axis versus short axis of ellipsoid more than 5:1, and (d) irregular voids that cannot be approximated by an ellipsoid shape. The defined ratios were selected to achieve meaningful classification of spherical, ellipsoidal, and lamellar voids as observed in Figs. 5d, 4b and 6d, and Fig. 7d respectively. More specific examples are presented in the appendix for both Mg and Ti.
2. Void orientation with respect to the loading direction. Void orientation plays an important role in the magnitude of local stress concentrations. In particular, stress intensity factors are proportional to the $sin^2(\alpha)$, where α is an angle between the loading axis and the long axis of the defect (void). The larger the angle, the higher the stress intensity factor. As the loading direction was horizontal on all presented images, ellipsoidal and especially lamellar voids oriented away from the loading direction can cause large concentrations. To quantify these aspects, we split a 360° circle into sectors corresponding to 0–30°, 30–60°, and 60–90° spreads from the loading direction. The schematic illustration of this approach is presented on Fig. 10. Here, the loading direction is horizontal, while a yellow dash line is plotted over the long axis of the void. In this given example,

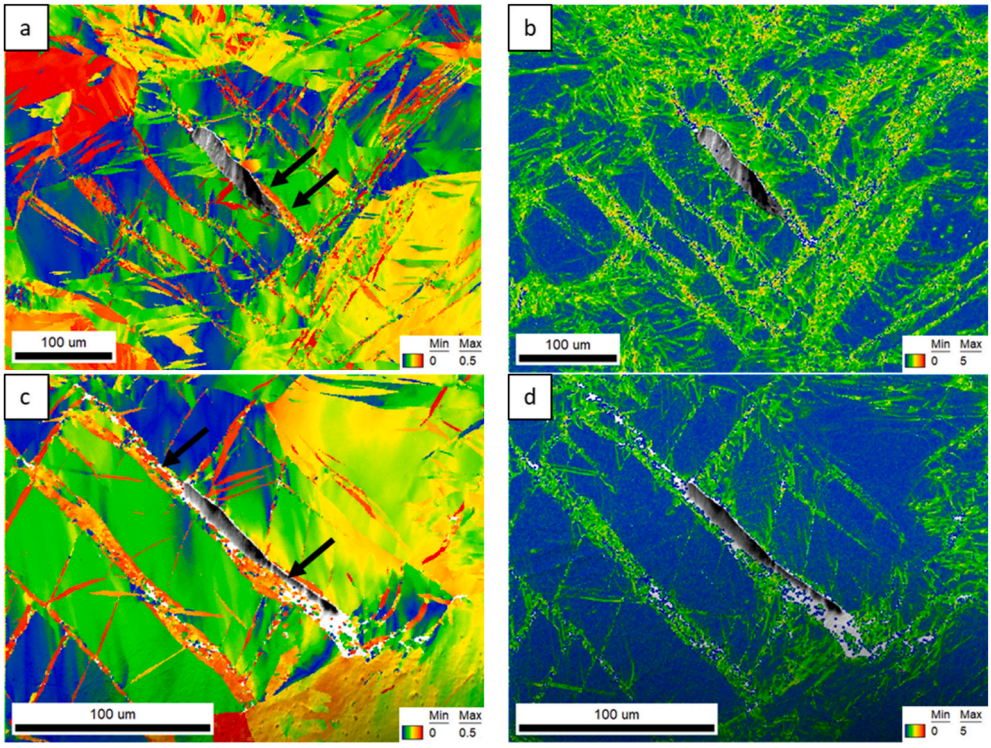

Fig. 8. (a,c) SF maps for basal slip and (b,d) KAM maps of areas around voids in Mg. (a,b) correspond to Fig. 6b and c and (c,d) correspond to Fig. 6d and e.

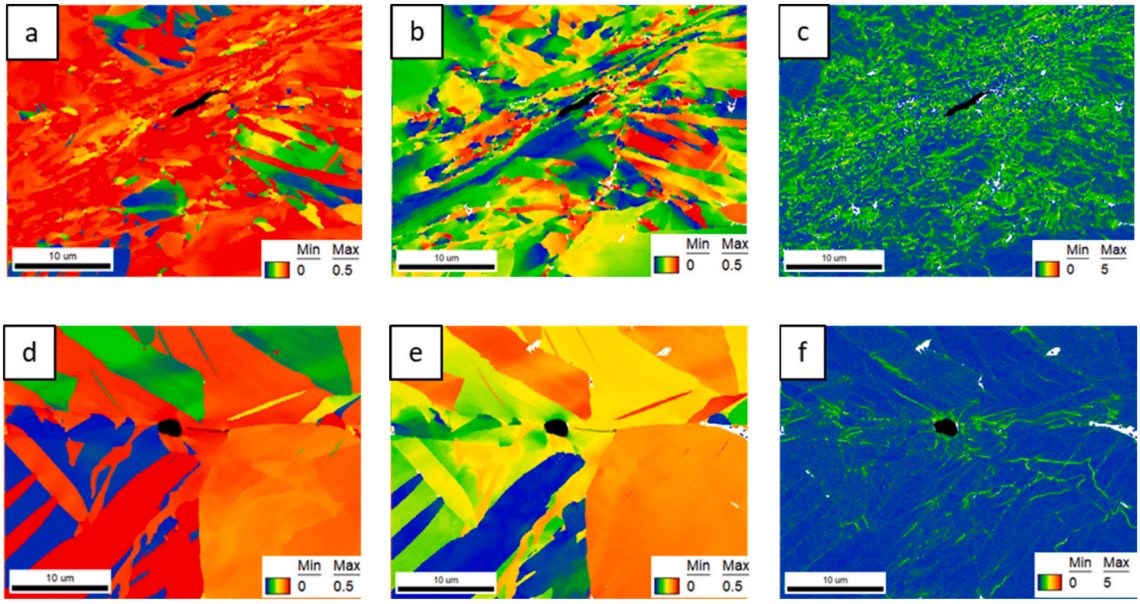

Fig. 9. (a,d) SF maps for prismatic slip (b,e) SF maps for basal slip, and (c,f) KAM maps of areas around voids in Ti. (a,b, and c) correspond to Fig. 5b and c and (d,e, and f) correspond to Fig. 5d and e.

the void belongs to the sector of 30–60° from the pull direction. This classification applies only to ellipsoidal and lamellar voids, as neither spherical nor irregular voids have a distinct long axis.

3. Number of twin families neighboring voids. Majority of voids neighbor twins of various families. In this parameter, we count the number of neighboring twin families around each void. As voids are often surrounded by 10–20 grain/twin fragments, it is difficult to statistically correlate each of these fragments to the void. Thus, rather than counting the number of neighboring twin lamellae, we count the number of neighboring twin modes/families. If at least one twin of a particular twin family neighbors a void, this is counted as an established presence of this twin family near the void.
4. Specific twin family neighboring voids.
5. Voids induced by a twin lamella and specific parent twin family for each lamellar void. Given that some voids have lamellar twin-like shape as in Fig. 6b–e and are located within twins or along a twin boundary, we count the number of these voids nucleated within twins (i.e. along the twin-matrix boundaries) and observe which twin family is a parent for each of these voids.

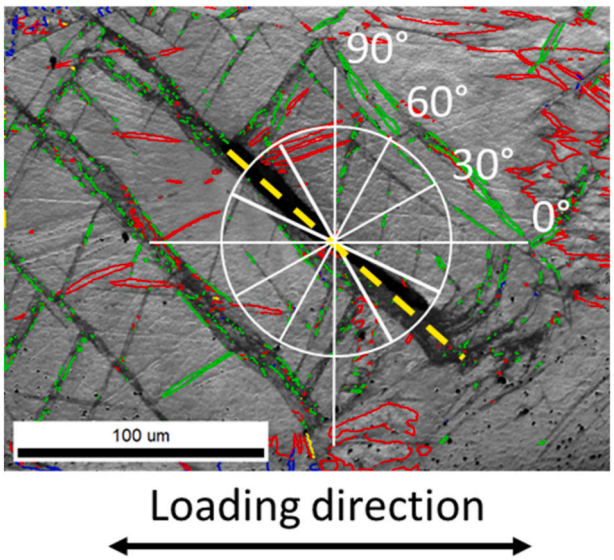

Fig. 10. Schematic illustration of the approach for calculation of orientation of ellipsoidal and lamellar voids with respect to the loading direction. The background image is presented in Fig. 6d and shows an IQ map with overlay of twin boundaries.

Observations of voids in pure Mg and Mg–3Zn alloy were grouped into a single category of Mg due to similarity of the observations in these materials. Although the Mg–3Zn alloy contains precipitates of the second phase MgZn, their content is very small, no more than 1%. Moreover, a typical size of these precipitates is a few tens to hundreds of nm which is small compared to the observed size of voids in Mg, ~100 μm. Thus, these fine precipitates in such a minor quantity are not expected to appreciably influence void nucleation in the Mg–3Zn alloy. No significant differences were observed between pure Mg and Mg–3Zn as supported by the third figure in the appendix. There was a total of 52 observations of voids in Mg and Mg–3Zn. These 52 observations were considered as 100%. Then, statistical distributions of the defined parameters are calculated from these 100%. For example, if 4 of voids in Mg are spherical, 8 are ellipsoidal, 16 are lamellar, and 24 are irregular, then the percentage of each group will be 7.6, 15.4, 30.8, and 46.2% respectively. Similar calculations are done for Ti where all 62 observations of voids are considered as 100% and split into groups (subcategories).

Fig. 11 presents the statistical distributions of void characteristics in Mg and Ti: void shape (Fig. 11a), void orientation for ellipsoidal and lamellar voids relative to the loading direction (Fig. 11b), number of twin systems neighboring voids (Fig. 11c), distribution of twin modes/families neighboring voids (Fig. 11d), and voids induced by twins of particular family (Fig. 11e).

Key observations from the statistical distributions in Fig. 11 can be summarized as follows:

(1) Fig. 11a: 61.5% of the voids in Mg have lamellar twin-like shape (such as shown in Fig. 6b–e and in the appendix for pure Mg) while 93.4% of voids in Ti voids are spherical and ellipsoidal (such as shown in Fig. 4b–e and Fig. 5d and e).
(2) Fig. 11b: 89.4% of ellipsoidal and lamellar voids in Mg are elongated in the direction greater than ±30° from the tension direction (Fig. 6b–e). Also, 36.8% of voids are elongated in the direction greater than ±60° from the tension direction. Some of the voids are elongated nearly 90° perpendicular to the loading direction as shown in the appendix. In contrast, the figure shows that 69.2% of ellipsoidal and lamellar voids in Ti are elongated in the direction within ±30° from the tension direction (Fig. 4b–c, Figure A4a-e).
(3) Fig. 11c: 92.3% of the voids in Mg and 83.3% voids in Ti neighbor twins of at least one family.
(4) Fig. 11d: 60% of twin families neighboring voids in Mg are extension twins {10–12} and 40% are compression twins {10–11}, while 43.9% of twin families neighboring voids in Ti are extension twins {10–12}, 41.5% are compression twins {11–22}, and 14.6% are extension twins {11–21}. Examples of these observations are presented in the appendix for both Mg and Ti.
(5) Fig. 11e: 53.8% of voids in Mg are induced by compression twins {10–11} (Fig. 6b–e) although extension twins are predominant neighbors, while 9.7% of voids in Ti are induced by twins of either extension {11–21} or extension {10–12} systems as depicted in the last figure of the appendix.

4. Discussion

This work is a statistical characterization study of voids formed in Mg and Ti under tension to near fracture. Local microstructures arounds 52 voids in Mg (pure Mg and Mg–3Zn alloy combined) and 62 voids in Ti were captured using EBSD mapping. Microstructures in the studied materials were adjusted to grains greater than 200 μm to magnify the phenomena. Nevertheless, fragments after deformation reduced down to μm and sub-μm scale due to profuse twinning and grain fragmentation. It is therefore no surprise that most of the voids in both Mg and Ti neighbor twins of at least one system.

Qualitative observations revealed that voids in Mg and Ti have different shape, size, and orientation. Voids in Ti are more round (Fig. 4b–e, Fig. 5d and e) with a small number of elongated voids within shear bands (Fig. 5b and c). The size of voids in Ti is typically within 10 μm. In contrast, multiple ellipsoidal or lamellar voids are observed in Mg that also resemble shape of lenticular twins (Fig. 6b–e) and have size reaching 100 μm. These voids elongate in the direction of microstructural features (twins) rather than in the pull direction. Ellipsoidal and lamellar voids in Ti are elongated predominantly in the direction within ±30° from the tension direction (Fig. 4b–c, Figure A4a-e). This is not the case with Mg in which some of the lamellar voids are nearly perpendicular to the loading direction as shown in the appendix.

Further analyses of SFs reveal that lamellar-shaped voids in Mg are located on the boundary between prior contraction twins with high SF for basal slip and parent grains with low SF for basal slip. Supported by conclusions from previous works [21,54,91–97], intense plastic deformation by basal slip within contraction twins and lack of slip transfer between the twin and parent grain due to low coherency leads to accumulation of dislocations followed by damage and decohesion at the twin-parent boundary. The intense plasticity within the twins leads to much higher KAM heterogeneity within twins than in parent grains, Fig. 8b and d. In contrast to Mg, correlations between SFs for basal and prismatic slip or KAM and location/properties of various voids in Ti were not obvious. While local correlations based on individual EBSD scans could be discussed, such considerations of multiple scans were controversial. For example, the void in Fig. 9c is located withing a region of a shear band with high KAM, while the void in Fig. 9e is located within a region with relative low KAM. Thus, these correlations were not expandable onto the entire dataset recorded for Ti. Certainly, voids in Ti are located in highly deformed regions in most of the cases as in Fig. 5b and c. Such highly deformed microstructures make quantitative analysis very complicated. Non-human judgment by Artificial Intelligence and Machine Learning can be attempted to establish correlations. Such works are left for the future.

Five parameters were used to classify statistical descriptions of 52 and 62 observed voids in Mg and Ti, respectively. Sufficient repeatability of the observed phenomena was ensured in the data. Therefore, the results can be regarded as homogenized properties of the materials. Describing phenomena in a quantitative way using such statistics and not only in a qualitative way facilitated several important insights, as summarized next.

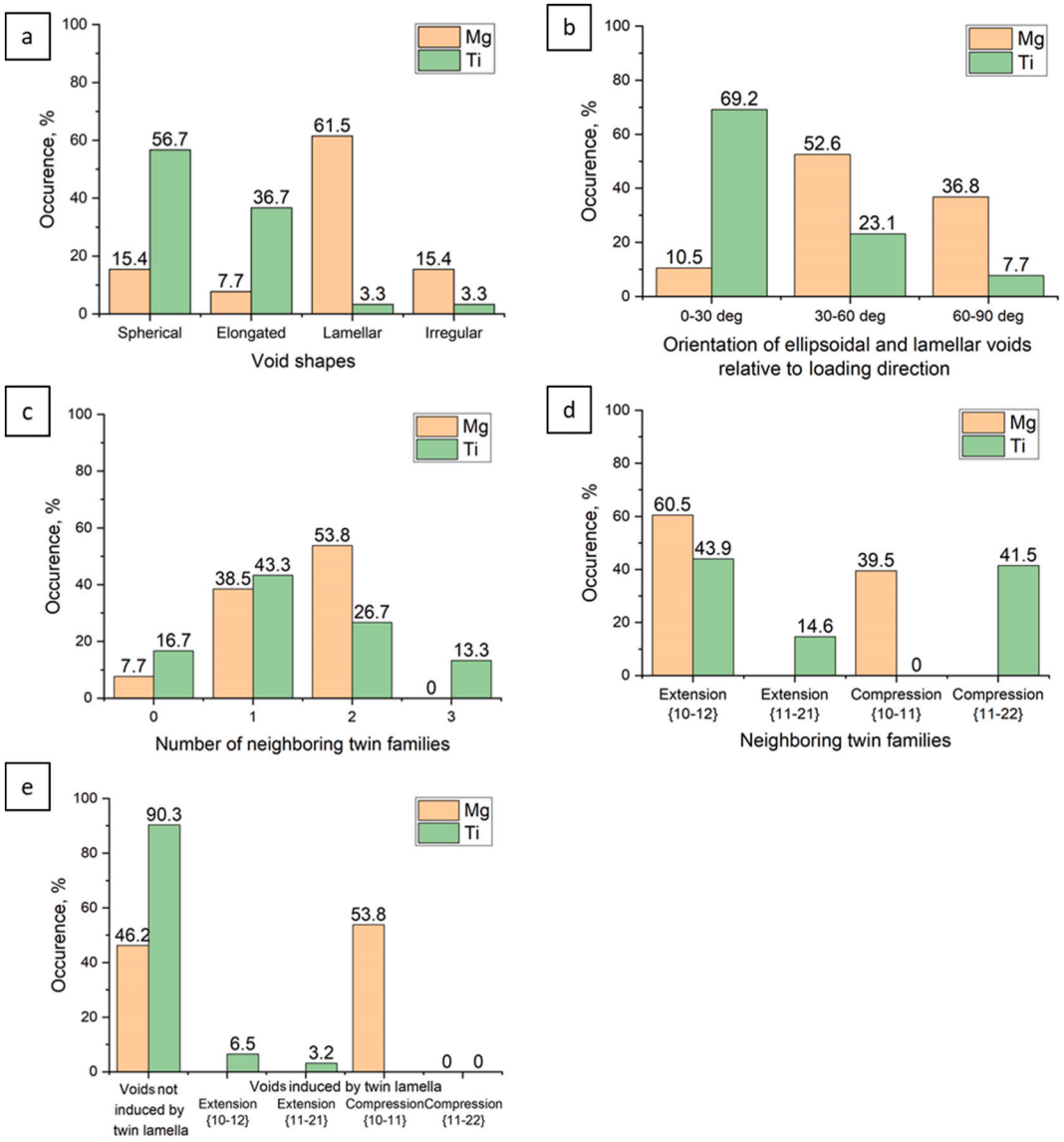

Fig. 11. Statistical distributions of void characteristic in Mg and Ti: (a) void shape, (b) void orientation for ellipsoidal and lamellar voids relative to the loading direction, (c) number of twin modes neighboring voids, (d) distribution of twin modes neighboring voids, (e) nucleation of voids induced by twin lamellae.

The present observations and conclusions are in good agreement with previous reports in the literature in terms of the location of voids in Mg. In Ref. [21], authors concluded that {10–11} twins can account for nucleation of lenticular twin-shaped voids and shear failure of magnesium at low strains. However, authors did not perform any statistical analysis on the fraction of these voids nucleated within twins. The present work complements these prior observations by providing statistics showing that up to 53.8% voids in Mg indeed nucleate within compression twins {10–11} highlighting the detrimental effects these twins play in damage formation and fracture of Mg.

In [54], multiple cylindrical/tubular voids were observed by X-ray tomography and attributed either to twinning or to intersecting slip planes. In the present work we show that 61.5% of the voids in Mg have lamellar twin-like shape, and 53.8% of voids nucleate within compression twins {10–11}. This shows that the lamellar voids predominantly nucleate within identified twins. As lamellar twins correlate with cylindrical/tubular shape in 3D, we can reliably state that majority of the tubular voids observed in Ref. [54] originated from twins and not intersecting slip planes. Isolated observations in Ref. [54] of twin-induced heterogeneities, lamellar-shaped voids, and pores at twin-grain boundaries are well supported and complimented by the present statistical observations, particularly, that 92% voids in Mg neighbor with twins of at least one system, and 53.8% of voids nucleate within twins. This makes a reliable conclusion that twinning highly influences nucleation and/or propagation of voids in Mg.

Nucleation and/or propagation of voids in Ti is moderately affected by twinning since 80.6% of voids neighbor with twins of at least one family. However, only 3.3% of voids have lamellar shape and only 9.7% are induced by twins of extension {10–12} or extension {11–21} systems. 56.7% of voids have spherical shape, while 69.2% of ellipsoidal

and lamellar voids are elongated in the direction within ±30° from pull direction but do not follow twin lamellae. The ellipsoidal and lamellar voids become elongated rather because of the sample shape change in the pull direction. Therefore, twinning only moderately influences voids in Ti. In contrast, microstructural evolution fragmenting grains and forming shear bands strongly influences voids in Ti as Ti is much more ductile than Mg.

The different nature of void nucleation evidently results in the dissimilar shape and orientation of voids in Mg and Ti. As voids in Mg predominantly nucleate along twins, which can cross entire grains, voids in Mg can be as large as grain size of the material and oriented along twinning boundaries. In comparison, highly fragmented microstructure of Ti with no apparent effect from twinning results in generation of rather small spherical voids which then elongate in the direction close to the macroscopic pull direction. Void size in Ti is essentially independent on the initial grain structure, as voids are observed only at latter stages of deformation where microstructure is heavily fragmented due to intense plasticity.

As evident from the derived statistical data and qualitative observations, voids in Mg have much more detrimental effect on the mechanical properties and fracture compared to Ti. Voids in Mg are much larger, often have sharp lamellar shape and oriented at high angles relative to pull direction. These factors lead to increase of local stress concentrations and earlier fracture. It is therefore no surprise that a material with such defects would have lower ductility compared the materials with smaller and more spherical voids. Even though we do not directly compare ductility of Ti and Mg as results of voids, it is evident that voids in Ti present a much better scenario for fracture properties compared to those in Mg.

5. Conclusions

In this work, we performed a statistical characterization study of voids formed in Mg and Ti under tension while correlating surrounding microstructures. Local microstructures were captured around 52 voids in Mg (pure Mg and Mg–3Zn alloy combined) and 62 voids in Ti using high-resolution EBSD mapping to form a comprehensive experimental dataset. In contrast to studies utilizing only a few observations, the work presented here ensured sufficient repeatability of the observed phenomena to form statistical distributions of shape of voids, orientation of voids with respect to the loading direction, number of twin modes neighboring voids, specific twin mode neighboring voids, and twinning lamellae induced voids. Thus, the results are averaged properties of the materials and not just locally observed phenomena. More correlations between void location/properties and surrounding microstructure can potentially be extracted from the dataset in the future with applications of artificial intelligence and machine learning techniques. The work established principal differences between voids in Mg and Ti with the main conclusions as follows:

- Voids in Ti are observed to be small in size (<10 μm) and predominantly spherical, while those in Mg are much bigger (~100 μm) and have predominantly lamellar shape. The minor content of ellipsoidal and lamellar voids in Ti are oriented along the loading direction, while major content of those voids in Mg are oriented away from the loading direction. Statistics including size, shape, and orientation of voids showed that voids in Mg have much higher stress concentration effects detrimental to fracture properties than those in Ti.
- Statistical distributions provided a quantitative support to a known concept that formation of voids in Mg is strongly dependent on existence of compression twins in the structure. These twins create lamellar voids in Mg and due to their shape and size strongly influence fracture properties. Suppression of contraction twinning or reducing the size of those twins can benefit fracture properties of the material due to the reduced effect of stress concentration. This also explains, besides other reasons, lower ductility of coarse-grained Mg alloys and enhanced ductility of the fine-grained ones.
- While twins moderately influence formation of voids in Ti, majority of voids result from substantial microstructural evolution to large strains including formation of shear bands. Unlike in Mg, no reliable correlations were established between location of voids and orientation of neighboring grains, SFs for basal or prismatic slip, and KAM in Ti, even though voids are located in highly deformed regions.

CRediT authorship contribution statement

Evgenii Vasilev: Methodology, Validation, Formal analysis, Investigation, Data curation, Writing – original draft. **Marko Knezevic:** Conceptualization, Methodology, Investigation, Resources, Writing – review & editing, Supervision, Project administration, Funding acquisition.

Declaration of competing interest

The authors declare that they have no known competing financial interests or personal relationships that could have appeared to influence the work reported in this paper.

Data availability

Data will be made available on request.

Acknowledgements

This research was sponsored by the U.S. National Science Foundation and was accomplished under the CAREER grant no. CMMI-1650641.

Appendix A

This appendix presents geometry of test specimens in Figure A1, SE SEM images showing sample preparation underneath the initial surface in Figure A2, voids in pure Mg in Figure A3, voids in pure Mg oriented nearly perpendicular to the loading direction in Figure A4, voids of different shape in Ti in Figure A5, voids of different shape in Mg in Figure A6, twin families adjacent to voids in Ti in Figure A7, twin families adjacent to voids in Mg in Figure A8, and twin-induced voids in Ti in Figure A9.

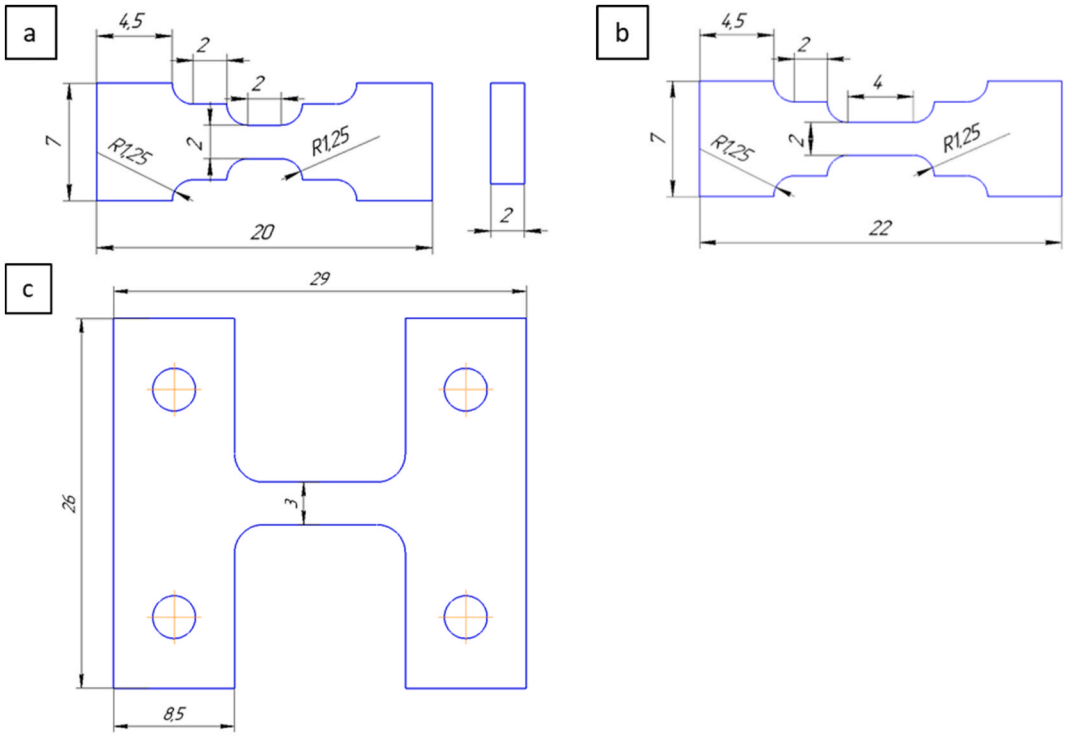

Fig. A1. Geometry of the tensile specimens used to test: (a) Mg–3Zn alloy, (b) pure Ti, and (c) pure Mg. Thickness of all specimens was 2 mm.

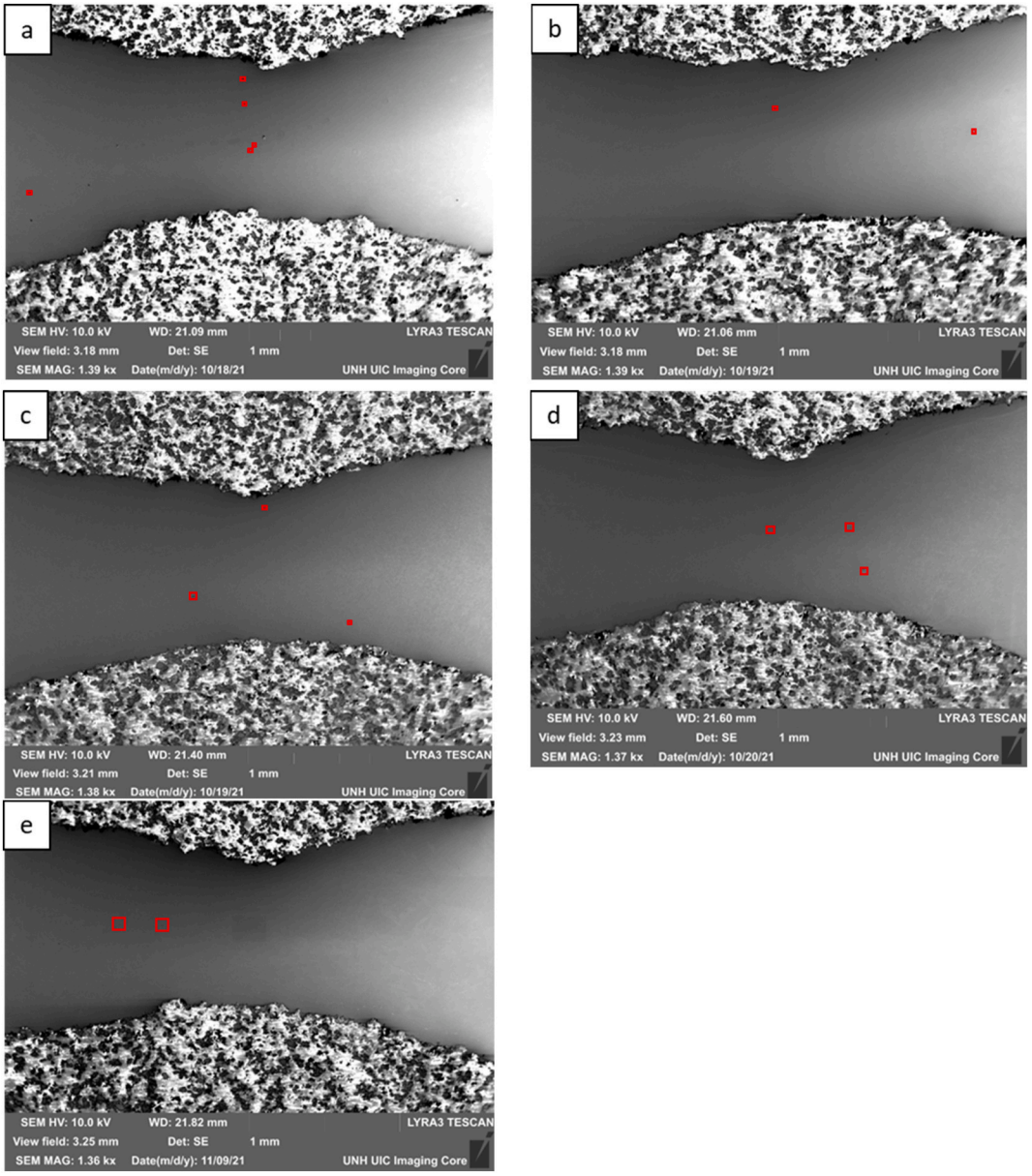

Fig. A2. SE SEM images of sample 1 at the engineering strain of 1.1 after: (a) initial polishing, (b-e) polishing to depths of 15, 25, 40, and 55 μm below the initial polishing surface in (a). Red squares highlight voids.

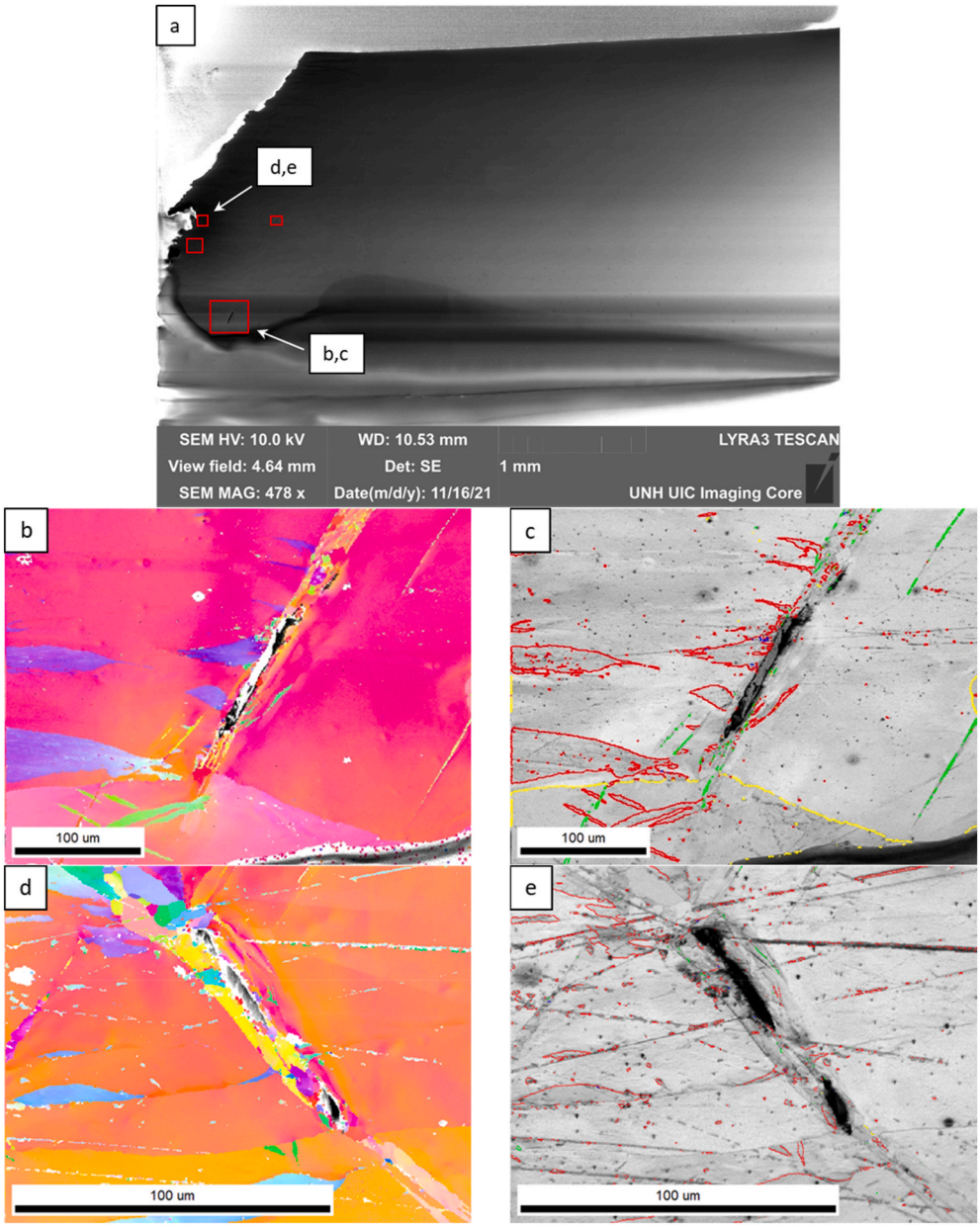

Fig. A3. Images of pure Mg showing similar looking voids as in Mg–3Zn alloy: (a) SEM image of the gauge section after tension to an engineering strain of 0.14 of pure Mg (sample 8). Red squares highlight locations of pores. (b,d) IPF maps of the areas around pores indicated in (a) and (c,e) corresponding IQ maps with overlays of twin boundaries.

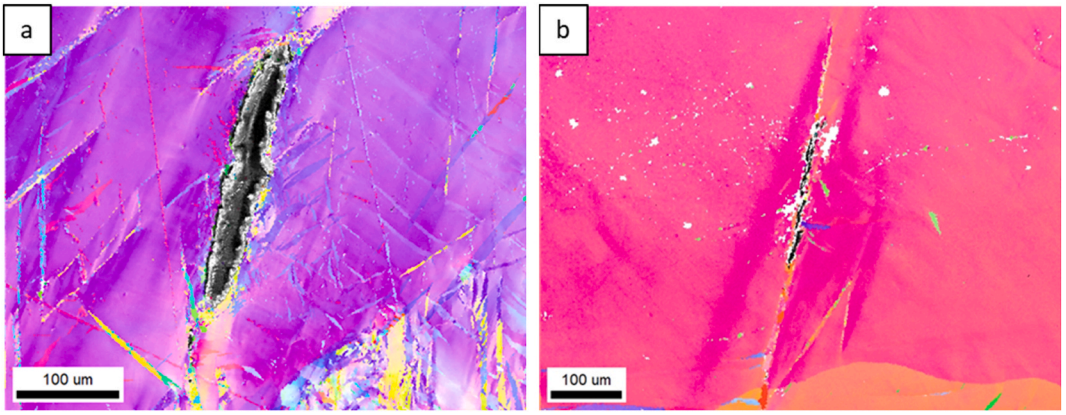

Fig. A4. Voids in pure Mg oriented nearly perpendicular to the loading direction, which is horizontal. Images are taken from: (a) sample 5 at an engineering strain of 0.22 and (b) sample 7 at an engineering strain of 0.15.

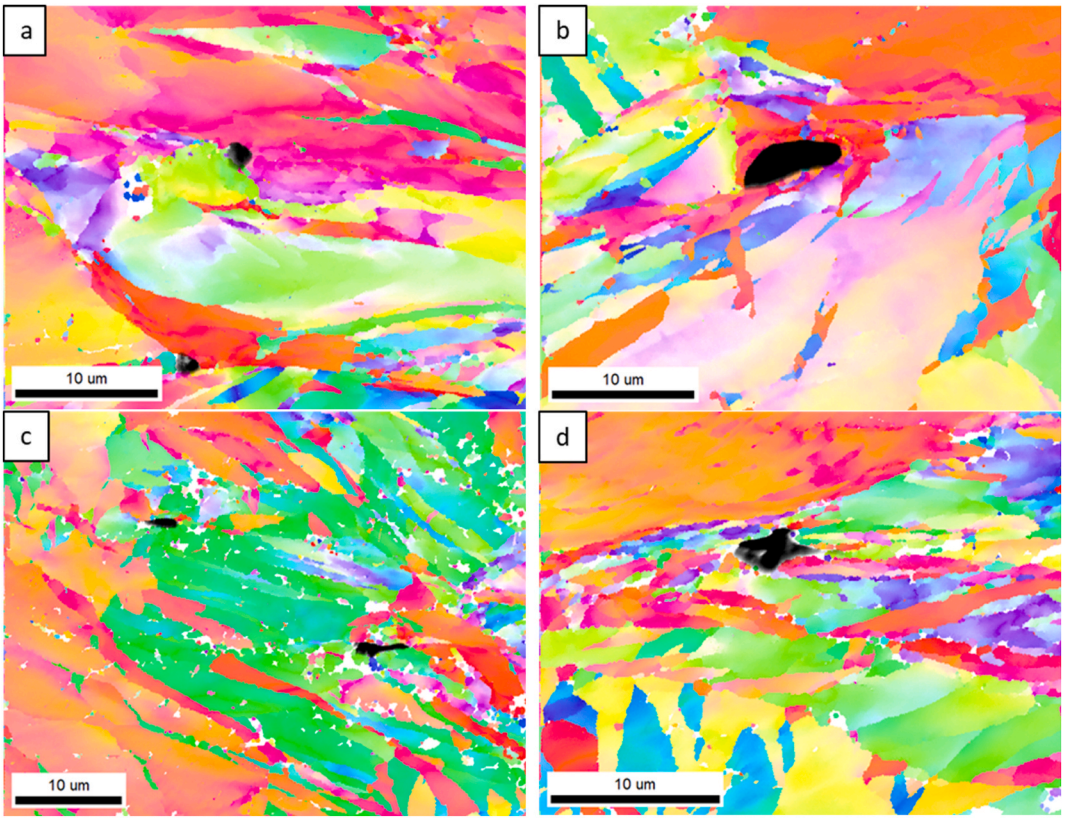

Fig. A5. IPF maps showing examples of: (a) spherical, (b) ellipsoidal, (c) lamellar, and (d) irregular-shaped voids in pure Ti. Images are taken from sample 1 deformed to an engineering strain of 1.1.

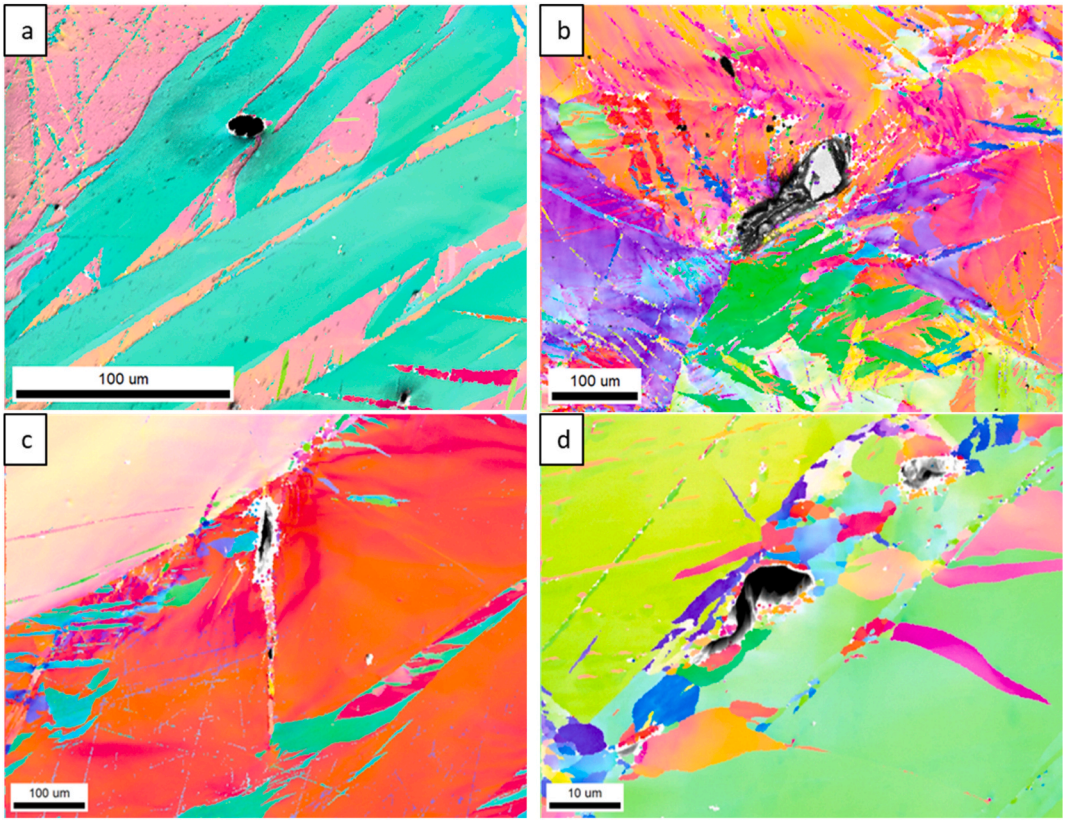

Fig. A6. IPF maps showing examples of: (a) spherical, (b) ellipsoidal, (c) lamellar, and (d) irregular-shaped voids in Mg. Images are taken from: (a) pure Mg at an engineering strain of 0.22 (sample 5), (b) Mg–3Zn at an engineering strain of 0.21 (sample 4), and (c,d) pure Mg at an engineering strain of 0.10 (sample 6).

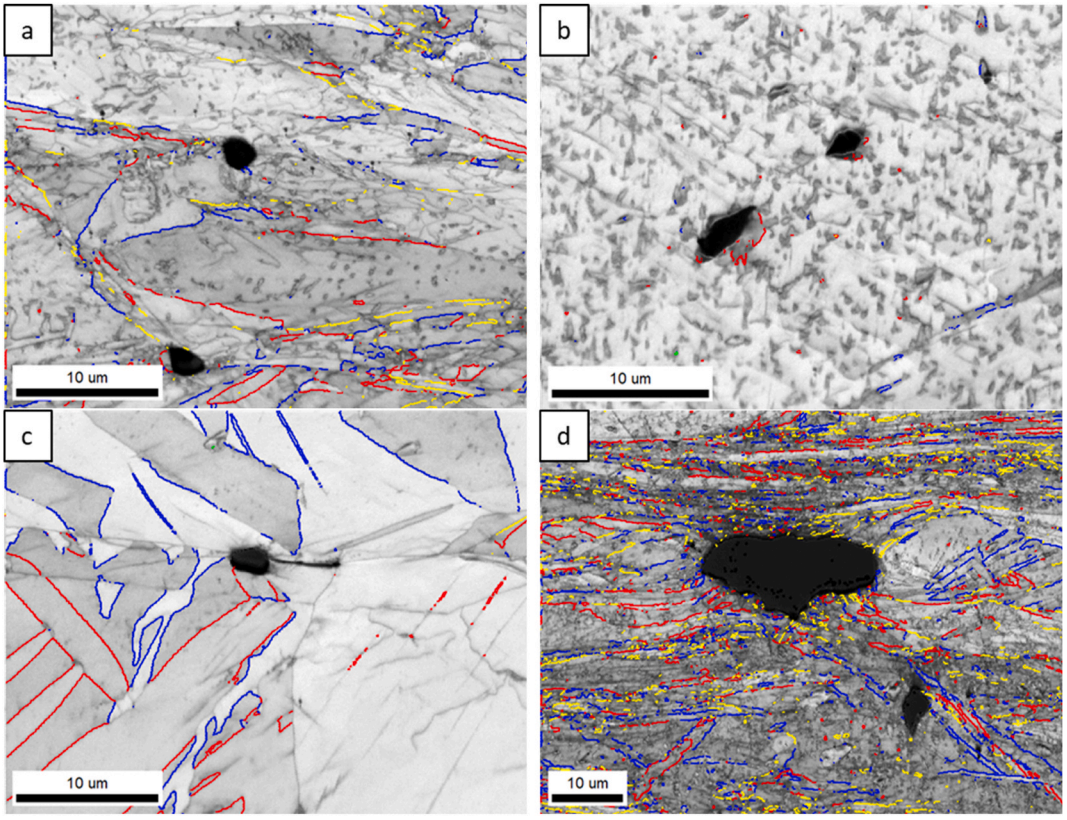

Fig. A7. IQ maps with overlay of twin boundaries illustrating different number of twin families adjacent to voids in Ti: (a) no neighboring twin families, (b) one neighboring twin family, $\{10\bar{1}2\}$, (c) two neighboring twin families, $\{10\bar{1}2\}$ and $\{10\bar{2}2\}$, (d) three neighboring twin families, $\{10\bar{1}2\}$, $\{10\bar{2}2\}$, and $\{10\bar{2}1\}$. Images are taken from (a-c) sample 1 at an engineering strain of 1.10 and (d) sample 2 at an engineering strain of 1.15.

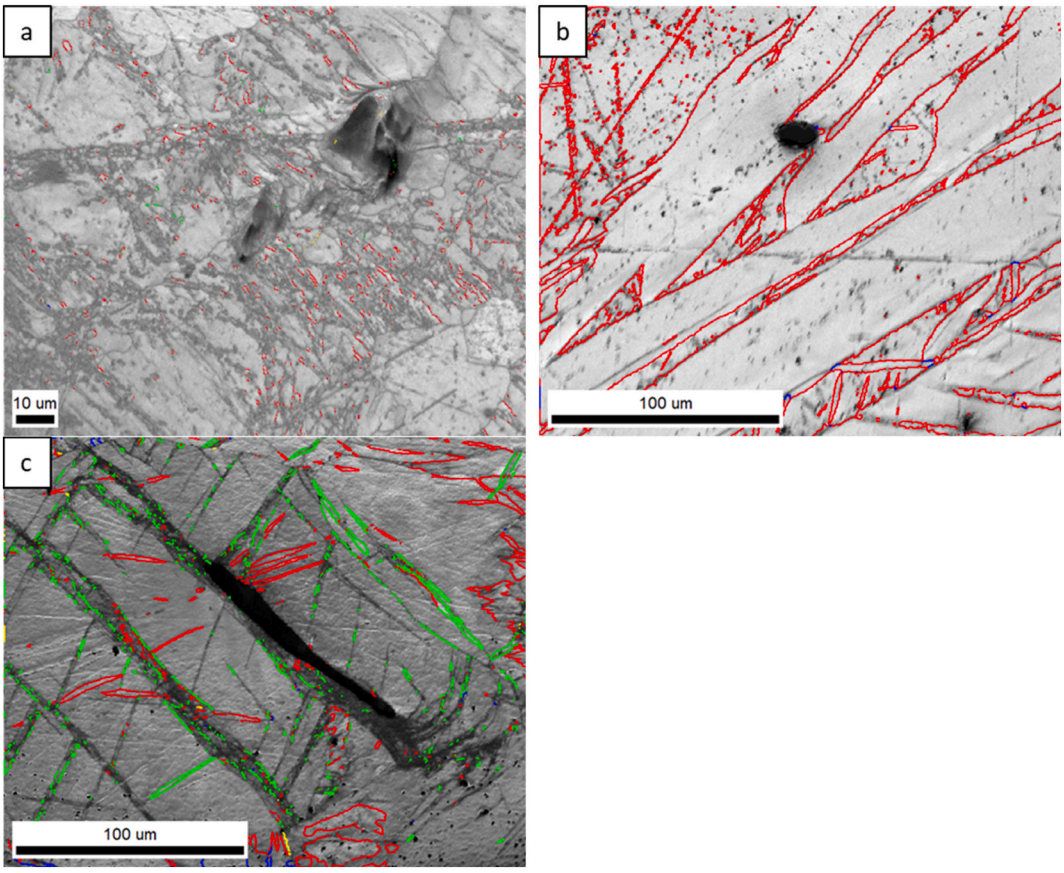

Fig. A8. –IQ maps with overlay of twin boundaries illustrating different number of twin families adjacent to voids in Mg: (a) no neighboring twin families, (b) one neighboring twin family, $\{10\bar{1}2\}$, (c) two neighboring twin families, $\{10\bar{1}2\}$ and $\{10\bar{1}1\}$. Images are taken from: (a) sample 7 at an engineering strain of 0.15, (b) sample 5 at an engineering strain of 0.22, and (c) sample 3 at an engineering strain of 0.24.

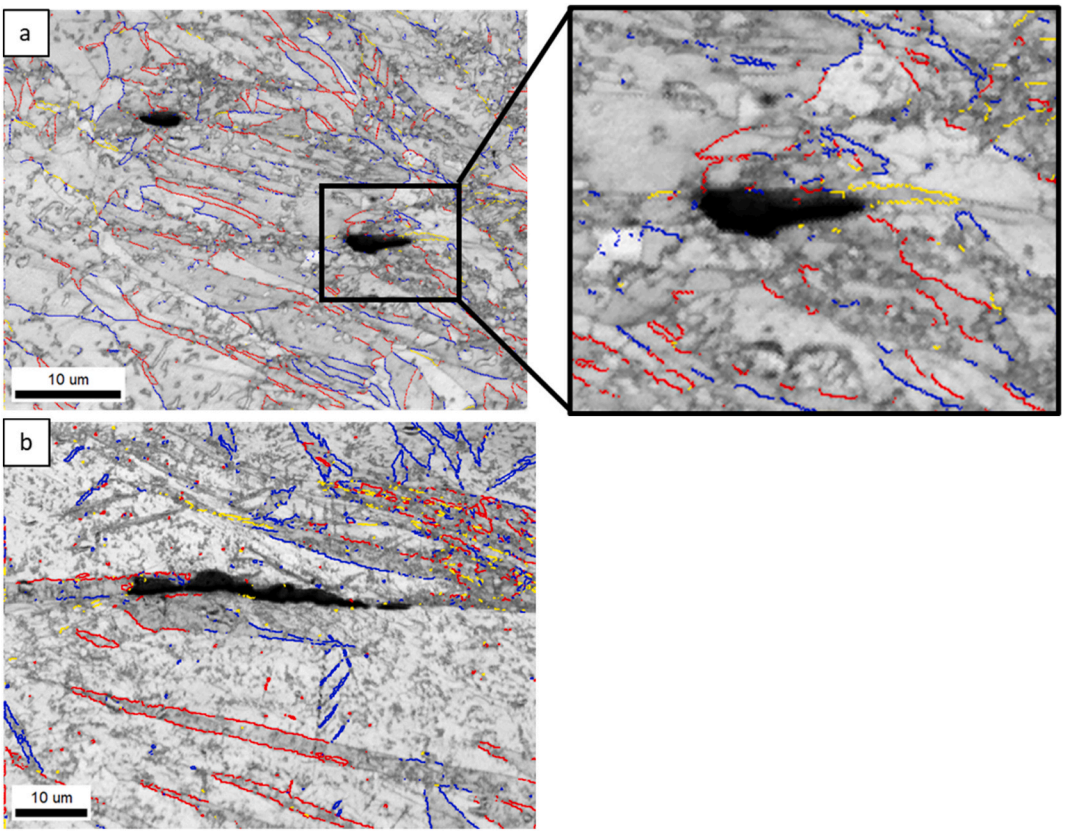

Fig. A9. IQ maps with overlay of twin boundaries illustrating twin-induced voids in Ti: (a) void induced by an extension twin $\{10\bar{2}1\}$ and (b) void induced by an extension twin $\{10\bar{1}2\}$. Images are taken from sample 1 at an engineering strain of 1.1.

References

[1] Z. Zhang, Y. Wu, F. Huang, Extension of a shear-controlled ductile fracture criterion by considering the necking coalescence of voids, Int. J. Solid Struct. (2022), https://doi.org/10.1016/j.ijsolstr.2021.111324.

[2] C.M. Poulin, Y.P. Korkolis, B.L. Kinsey, M. Knezevic, Over five-times improved elongation-to-fracture of dual-phase 1180 steel by continuous-bending-under-tension, Mater. Des. 161 (2019), https://doi.org/10.1016/j.matdes.2018.11.022.

[3] C.M. Poulin, T.J. Barrett, M. Knezevic, Inferring post-necking strain hardening behavior of sheets by a combination of continuous bending under tension testing and finite element modeling, Exp. Mech. 60 (4) (2020) 459–473, https://doi.org/10.1007/s11340-019-00577-1.

[4] K.E. Puttick, Ductile fracture in metals, Philos. Mag. A (1959), https://doi.org/10.1080/14786435908238272.

[5] T.L. Anderson, Fracture Mechanics: Fundamentals and Applications, fourth ed., 2017.

[6] D.J. Savage, O. Cazacu, M. Knezevic, Dilational response of voided polycrystals, JOM 69 (5) (2017) 942–947, https://doi.org/10.1007/s11837-017-2256-3.

[7] D.J. Savage, N. Chandola, O. Cazacu, B.A. McWilliams, M. Knezevic, Validation of recent analytical dilatational models for porous polycrystals using crystal plasticity finite element models with Schmid and non-Schmid activation laws, Mech. Mater. 126 (2018) 148–162, https://doi.org/10.1016/j.mechmat.2018.08.004.

[8] S.H. Goods, L.M. Brown, Overview No. 1. The nucleation of cavities by plastic deformation, Acta Metall. (1979), https://doi.org/10.1016/0001-6160(79)90051-8.

[9] T.C. Lindley, G. Oates, C.E. Richards, Fibre-loading mechanism for the fracture of cementite films in ferrite, Nature (1970), https://doi.org/10.1038/226145a0.

[10] P.J. Noell, J.E.C. Sabisch, D.L. Medlin, B.L. Boyce, Nanoscale conditions for ductile void nucleation in copper: vacancy condensation and the growth-limited microstructural state, Acta Mater. (2020), https://doi.org/10.1016/j.actamat.2019.11.022.

[11] M. Ardeljan, M. Knezevic, T. Nizolek, I.J. Beyerlein, N.A. Mara, T.M. Pollock, A study of microstructure-driven strain localizations in two-phase polycrystalline HCP/BCC composites using a multi-scale model, Int. J. Plast. 74 (2015) 35–57, https://doi.org/10.1016/j.ijplas.2015.06.003.

[12] M. Jahedi, M. Ardeljan, I.J. Beyerlein, M.H. Paydar, M. Knezevic, Enhancement of orientation gradients during simple shear deformation by application of simple compression, J. Appl. Phys. 117 (21) (2015), 214309, https://doi.org/10.1063/1.4922032.

[13] M. Jahedi, E. Ardjmand, M. Knezevic, Microstructure metrics for quantitative assessment of particle size and dispersion: application to metal-matrix composites, Powder Technol. 311 (2017) 226–238, https://doi.org/10.1016/j.powtec.2017.01.093.

[14] M.J. Nemcko, D.S. Wilkinson, On the damage and fracture of commercially pure magnesium using x-ray microtomography, Mater. Sci. Eng., A (2016), https://doi.org/10.1016/j.msea.2016.08.095.

[15] J.N. Greenwood, D.R. Miller, J.W. Suiter, Intergranular cavitation in stressed metals, Acta Metall. (1954), https://doi.org/10.1016/0001-6160(54)90166-2.

[16] M. Jahedi, B.A. McWilliams, M. Knezevic, Deformation and fracture mechanisms in WE43 magnesium-rare earth alloy fabricated by direct-chill casting and rolling, Mater. Sci. Eng., A 726 (2018) 194–207, https://doi.org/10.1016/j.msea.2018.04.090.

[17] D. Wu, L. Liu, L. Zhang, W. Wang, K. Zhou, Tensile deformation mechanism and micro-void nucleation of Ti-55531 alloy with bimodal microstructure, J. Mater. Res. Technol. (2020), https://doi.org/10.1016/j.jmrt.2020.11.008.

[18] D. Qin, Y. Lu, D. Guo, L. Zheng, Q. Liu, L. Zhou, Tensile deformation and fracture of Ti-5Al-5V-5Mo-3Cr-1.5Zr-0.5Fe alloy at room temperature, Mater. Sci. Eng., A (2013), https://doi.org/10.1016/j.msea.2013.08.055.

[19] Y. Krishna Mohan Rao, V.V. Kutumbarao, P. Rama Rao, Influence of microstructure on void nucleation and growth in a near-α titanium alloy IMI 685, Mater. Sci. Eng., A (1989), https://doi.org/10.1016/0921-5093(89)90170-6.

[20] C.M. Poulin, S.C. Vogel, Y.P. Korkolis, B.L. Kinsey, M. Knezevic, Experimental studies into the role of cyclic bending during stretching of dual-phase steel sheets, Int. J. Material Form. 13 (3) (2020) 393–408, https://doi.org/10.1007/s12289-019-01530-2.

[21] M.R. Barnett, Twinning and the ductility of magnesium alloys: Part II. 'Contraction' twins [Online], Mater. Sci. Eng., A 464 (1–2) (2007) 8–16, http://www.sciencedirect.com/science/article/B6TXD-4N5TN8C-4/2/3ea750c9e55aef479f8f62380676defc.

[22] M. Ardeljan, I.J. Beyerlein, B.A. McWilliams, M. Knezevic, Strain rate and temperature sensitive multi-level crystal plasticity model for large plastic deformation behavior: application to AZ31 magnesium alloy, Int. J. Plast. 83 (2016) 90–109, https://doi.org/10.1016/j.ijplas.2016.04.005.

[23] M. Ardeljan, R.J. McCabe, I.J. Beyerlein, M. Knezevic, Explicit incorporation of deformation twins into crystal plasticity finite element models, Comput. Methods Appl. Mech. Eng. 295 (2015) 396–413, https://doi.org/10.1016/j.cma.2015.07.003.

[24] J. Samei, et al., 4D X-ray tomography characterization of void nucleation and growth during deformation of strontium-added AZ31 alloys, Mater. Sci. Eng., A (2020), https://doi.org/10.1016/j.msea.2020.140081.
[25] C.D. Calhoun, N.S. Stoloff, The effects of particles on fracture processes in magnesium alloys, Metall. Trans. A (1970), https://doi.org/10.1007/BF02811784.
[26] N. Kanetake, M. Nomura, T. Choh, Continuous observation of microstructural degradation during tensile loading of particle reinforced aluminium matrix composites, Mater. Sci. Technol. (2012), https://doi.org/10.1179/026708395790164599.
[27] M. Jahedi, M.H. Paydar, M. Knezevic, Enhanced microstructural homogeneity in metal-matrix composites developed under high-pressure-double-torsion, 0, Mater. Char. 104 (2015) 92–100, https://doi.org/10.1016/j.matchar.2015.04.012.
[28] H. Zare, M. Jahedi, M.R. Toroghinejad, M. Meratian, M. Knezevic, Microstructure and mechanical properties of carbon nanotubes reinforced aluminum matrix composites synthesized via equal-channel angular pressing, Mater. Sci. Eng., A 670 (2016) 205–216, https://doi.org/10.1016/j.msea.2016.06.027.
[29] H. Zare, M. Jahedi, M.R. Toroghinejad, M. Meratian, M. Knezevic, Compressive, shear, and fracture behavior of CNT reinforced Al matrix composites manufactured by severe plastic deformation, Mater. Des. 106 (2016) 112–119, https://doi.org/10.1016/j.matdes.2016.05.109.
[30] C.L. Briant, Z.F. Wang, N. Chollocoop, Hydrogen embrittlement of commercial purity titanium, Corrosion Sci. (2002), https://doi.org/10.1016/S0010-938X(01)00159-7.
[31] B. Wierzba, Competition between Kirkendall and Frenkel effects during multicomponent interdiffusion process, Phys. A Stat. Mech. its Appl. (2014), https://doi.org/10.1016/j.physa.2014.02.014.
[32] A.M. Gusak, T.V. Zaporozhets, Hollow nanoshell formation and collapse in binary solid solutions with large range of solubility, J. Phys. Condens. Matter (2009), https://doi.org/10.1088/0953-8984/21/41/415303.
[33] C.K.C. Lieou, C.A. Bronkhorst, Dynamic recrystallization in adiabatic shear banding: effective-temperature model and comparison to experiments in ultrafine-grained titanium, Int. J. Plast. 111 (Dec. 2018) 107–121, https://doi.org/10.1016/J.IJPLAS.2018.07.011.
[34] Y. Cui, Z. Chen, Void initiation from interfacial debonding of spherical silicon particles inside a silicon-copper nanocomposite: a molecular dynamics study, Model. Simulat. Mater. Sci. Eng. (2017), https://doi.org/10.1088/1361-651X/aa51e5.
[35] H.G.F. Wilsdorf, The ductile fracture of metals: a microstructural viewpoint, Mater. Sci. Eng. 59 (1) (1983) 1–39, https://doi.org/10.1016/0025-5416(83)90085-X.
[36] R.N. Gardner, T.C. Pollock, H.G.F. Wilsdorf, Crack initiation at dislocation cell boundaries in the ductile fracture of metals, Mater. Sci. Eng. (1977), https://doi.org/10.1016/0025-5416(77)90123-9.
[37] H.G.F. Wilsdorf, The role of glide and twinning in the final separation of ruptured gold crystals, Acta Metall. (1982), https://doi.org/10.1016/0001-6160(82)90021-9.
[38] M. Knezevic, et al., Modeling bending of α-titanium with embedded polycrystal plasticity in implicit finite elements, 0, Mater. Sci. Eng., A 564 (2013) 116–126, https://doi.org/10.1016/j.msea.2012.11.037.
[39] M. Wronski, M. Arul Kumar, L. Capolungo, R.J. McCabe, K. Wierzbanowski, C. N. Tomé, Deformation behavior of CP-titanium: experiment and crystal plasticity modeling, Mater. Sci. Eng., A (2018), https://doi.org/10.1016/j.msea.2018.03.017.
[40] M. Ardeljan, I.J. Beyerlein, M. Knezevic, Effect of dislocation density-twin interactions on twin growth in AZ31 as revealed by explicit crystal plasticity finite element modeling, Int. J. Plast. 99 (Supplement C) (2017) 81–101, https://doi.org/10.1016/j.ijplas.2017.09.002.
[41] T.J. Barrett, R.J. McCabe, D.W. Brown, B. Clausen, S.C. Vogel, M. Knezevic, Predicting deformation behavior of α-uranium during tension, compression, load reversal, rolling, and sheet forming using elasto-plastic, multi-level crystal plasticity coupled with finite elements, J. Mech. Phys. Solid. 138 (2020), 103924, https://doi.org/10.1016/j.jmps.2020.103924.
[42] M. Zecevic, M. Knezevic, I.J. Beyerlein, C.N. Tomé, An elasto-plastic self-consistent model with hardening based on dislocation density, twinning and de-twinning: application to strain path changes in HCP metals, 0, Mater. Sci. Eng., A 638 (2015) 262–274, https://doi.org/10.1016/j.msea.2015.04.066.
[43] M. Knezevic, I.J. Beyerlein, D.W. Brown, T.A. Sisneros, C.N. Tomé, A polycrystal plasticity model for predicting mechanical response and texture evolution during strain-path changes: application to beryllium, 0, Int. J. Plast. 49 (2013) 185–198, https://doi.org/10.1016/j.ijplas.2013.03.008.
[44] M. Knezevic, et al., Anisotropic stress-strain response and microstructure evolution of textured a-uranium [Online], Acta Mater. 60 (2) (2012) 702–715, http://www.sciencedirect.com/science/article/pii/S1359645411007464.
[45] C.C. Aydiner, M.A. Telemez, Multiscale deformation heterogeneity in twinning magnesium investigated with in situ image correlation, Int. J. Plast. (2014), https://doi.org/10.1016/j.ijplas.2013.12.001.
[46] M. Yaghoobi, Z. Chen, A.D. Murphy-Leonard, V. Sundararaghavan, S. Daly, J. E. Allison, Deformation twinning and detwinning in extruded Mg-4Al: in-situ experiment and crystal plasticity simulation, Int. J. Plast. 155 (Aug. 2022), 103345, https://doi.org/10.1016/J.IJPLAS.2022.103345.
[47] W. Li, Y. Jing, T. Zhou, G. Xing, A new ductile fracture model for structural metals considering effects of stress state, strain hardening and micro-void shape, Thin-Walled Struct. 176 (Jul. 2022), 109280, https://doi.org/10.1016/J.TWS.2022.109280.
[48] B.J. Lee, M.E. Mear, Axisymmetric deformation of power-law solids containing a dilute concentration of aligned spheroidal voids, J. Mech. Phys. Solid. (1992), https://doi.org/10.1016/0022-5096(92)90052-4.
[49] M. Knezevic, B. Drach, M. Ardeljan, I.J. Beyerlein, Three dimensional predictions of grain scale plasticity and grain boundaries using crystal plasticity finite element models, 0, Comput. Methods Appl. Mech. Eng. 277 (2014) 239–259, https://doi.org/10.1016/j.cma.2014.05.003.
[50] T. Pardoen, J.W. Hutchinson, An extended model for void growth and coalescence, J. Mech. Phys. Solid. 48 (12) (2000) 2467–2512.
[51] A.R. Ragab, Application of an extended void growth model with strain hardening and void shape evolution to ductile fracture under axisymmetric tension, Eng. Fract. Mech. (2004), https://doi.org/10.1016/S0013-7944(03)00216-9.
[52] F. Scheyvaerts, P.R. Onck, C. Tekoğlu, T. Pardoen, The growth and coalescence of ellipsoidal voids in plane strain under combined shear and tension, J. Mech. Phys. Solid. (2011), https://doi.org/10.1016/j.jmps.2010.10.003.
[53] C.E. Inglis, Stress in a plate due to the presence of cracks and sharp corners, Spring Meetings of the Fifty-fourth Session of the Institution of Naval Architects (1913) 219–241.
[54] E. Vasilev, M. Knezevic, Role of microstructural heterogeneities in damage formation and fracture of oligocrystalline Mg under tensile loading, Mater. Sci. Eng., A (2021), https://doi.org/10.1016/j.msea.2021.142096.
[55] N. Ali, L. Zhang, H. Zhou, A. Zhao, C. Zhang, Y. Gao, Elucidation of void defects by soft reduction in medium carbon steel via EBSD and X-ray computed tomography, Mater. Des. (2021), https://doi.org/10.1016/j.matdes.2021.109978.
[56] J.P.M. Hoefnagels, C.C. Tasan, F. Maresca, F.J. Peters, V.G. Kouznetsova, Retardation of plastic instability via damage-enabled microstrain delocalization, J. Mater. Sci. (2015), https://doi.org/10.1007/s10853-015-9164-0.
[57] T.W.J. de Geus, J.E.P. van Duuren, R.H.J. Peerlings, M.G.D. Geers, Fracture initiation in multi-phase materials: a statistical characterization of microstructural damage sites, Mater. Sci. Eng., A (2016), https://doi.org/10.1016/j.msea.2016.06.082.
[58] C.F. Kusche, F. Pütz, S. Münstermann, T. Al-Samman, S. Korte-Kerzel, On the effect of strain and triaxiality on void evolution in a heterogeneous microstructure – a statistical and single void study of damage in DP800 steel, Mater. Sci. Eng., A (2021), https://doi.org/10.1016/j.msea.2020.140332.
[59] B. Epstein, Statistical aspects of fracture problems, J. Appl. Phys. (1948), https://doi.org/10.1063/1.1698380.
[60] K. Wallin, T. Saario, K. Törrönen, Statistical model for carbide induced brittle fracture in steel, Met. Sci. (1984), https://doi.org/10.1179/030634584790420384.
[61] T. Francis, et al., Multimodal 3D characterization of voids in shock-loaded tantalum: implications for ductile spallation mechanisms, Acta Mater. (2021), https://doi.org/10.1016/j.actamat.2021.117057.
[62] M. Arul Kumar, M. Wroński, R.J. McCabe, L. Capolungo, K. Wierzbanowski, C. N. Tomé, Role of microstructure on twin nucleation and growth in HCP titanium: a statistical study, Acta Mater. (2018), https://doi.org/10.1016/j.actamat.2018.01.041.
[63] L. Lecarme, et al., Heterogenous void growth revealed by in situ 3-D X-ray microtomography using automatic cavity tracking, Acta Mater. (2014), https://doi.org/10.1016/j.actamat.2013.10.014.
[64] N.C. Ferreri, S.C. Vogel, M. Knezevic, Determining volume fractions of γ, γ′, γ″, δ, and MC-carbide phases in Inconel 718 as a function of its processing history using an advanced neutron diffraction procedure, Mater. Sci. Eng., A 781 (2020), 139228, https://doi.org/10.1016/j.msea.2020.139228.
[65] S. Gribbin, S. Ghorbanpour, N.C. Ferreri, J. Bicknell, I. Tsukrov, M. Knezevic, Role of grain structure, grain boundaries, crystallographic texture, precipitates, and porosity on fatigue behavior of Inconel 718 at room and elevated temperatures, Mater. Char. 149 (2019) 184–197, https://doi.org/10.1016/j.matchar.2019.01.028.
[66] Advanced Light Alloys and Composites, 1998, https://doi.org/10.1007/978-94-015-9068-6.
[67] H.M. Flower, Light alloys: metallurgy of the light metals, Int. Mater. Rev. (2012), https://doi.org/10.1179/095066092790150876.
[68] I.A. Riyad, et al., Modeling the role of local crystallographic correlations in microstructures of Ti-6Al-4V using a correlated structure visco-plastic self-consistent polycrystal plasticity formulation, Acta Mater. 203 (2021), 116502, https://doi.org/10.1016/j.actamat.2020.116502.
[69] M. Knezevic, et al., Thermo-hydrogen refinement of microstructure to improve mechanical properties of Ti–6Al–4V fabricated via laser powder bed fusion, Mater. Sci. Eng., A 809 (2021), 140980, https://doi.org/10.1016/j.msea.2021.140980.
[70] M. Zecevic, I.J. Beyerlein, M. Knezevic, Coupling elasto-plastic self-consistent crystal plasticity and implicit finite elements: applications to compression, cyclic tension-compression, and bending to large strains, Int. J. Plast. 93 (2017) 187–211, https://doi.org/10.1016/j.ijplas.2016.07.016.
[71] J. Wang, et al., Origins of high ductility exhibited by an extruded magnesium alloy Mg-1.8Zn-0.2Ca: experiments and crystal plasticity modeling, J. Mater. Sci. Technol. 84 (2021) 27–42, https://doi.org/10.1016/j.jmst.2020.12.047.
[72] E. Vasilev, N.C. Ferreri, R. Decker, I.J. Beyerlein, M. Knezevic, Strain-Rate sensitivity, tension-compression asymmetry, r-ratio, twinning, and texture evolution of a rolled magnesium alloy Mg-1.3Zn-0.4Ca-0.4Mn, Metall. Mater. Trans. A 51 (8) (2020) 3858–3868, https://doi.org/10.1007/s11661-020-05841-x.
[73] B. Leu, et al., Processing of dilute Mg–Zn–Mn–Ca alloy/Nb multilayers by accumulative roll bonding, Adv. Eng. Mater. 22 (1) (2020), 1900673, https://doi.org/10.1002/adem.201900673.
[74] M.E. Alam, S. Pal, R. Decker, N.C. Ferreri, M. Knezevic, I.J. Beyerlein, Rare-earth- and aluminum-free, high strength dilute magnesium alloy for Biomedical Applications, Sci. Rep. 10 (1) (2020), 15839, https://doi.org/10.1038/s41598-020-72374-z.

[75] N.C. Ferreri, D.J. Savage, M. Knezevic, Non-acid, alcohol-based electropolishing enables high-quality electron backscatter diffraction characterization of titanium and its alloys: application to pure Ti and Ti-6Al-4V, Mater. Char. 166 (2020), 110406, https://doi.org/10.1016/j.matchar.2020.110406.
[76] Z. Zhao, M. Ramesh, D. Raabe, A.M. Cuitiño, R. Radovitzky, Investigation of three-dimensional aspects of grain-scale plastic surface deformation of an aluminum oligocrystal, Int. J. Plast. 24 (12) (2008) 2278–2297, https://doi.org/10.1016/j.ijplas.2008.01.002.
[77] E. Demir, I. Gutierrez-Urrutia, Investigation of strain hardening near grain boundaries of an aluminum oligocrystal: experiments and crystal based finite element method, Int. J. Plast. (2021), https://doi.org/10.1016/j.ijplas.2020.102898.
[78] D. Raabe, M. Sachtleber, H. Weiland, G. Scheele, Z. Zhao, Grain-scale micromechanics of polycrystal surfaces during plastic straining, Acta Mater. 51 (6) (2003) 1539–1560, https://doi.org/10.1016/s1359-6454(02)00557-8.
[79] N. Zhang, W. Tong, An experimental study on grain deformation and interactions in an Al-0. 5%Mg multicrystal, Int. J. Plast. (2004), https://doi.org/10.1016/S0749-6419(03)00100-1.
[80] A. Akhtar, E. Teghtsoonian, Solid solution strengthening of magnesium single crystals—I alloying behaviour in basal slip, Acta Metall. 17 (11) (1969) 1339–1349, https://doi.org/10.1016/0001-6160(69)90151-5.
[81] W.F. Hosford, Mechanical Behavior of Materials, 2005, https://doi.org/10.1017/CBO9780511810930.
[82] I. Chelladurai, et al., Modeling of trans-grain twin transmission in AZ31 via a neighborhood-based viscoplastic self-consistent model, Int. J. Plast. 117 (2019) 21–32, https://doi.org/10.1016/j.ijplas.2018.03.012.
[83] M. Risse, M. Lentz, C. Fahrenson, W. Reimers, M. Knezevic, I.J. Beyerlein, Elevated temperature effects on the plastic anisotropy of an extruded Mg-4 Wt pct Li alloy: experiments and polycrystal modeling, Metall. Mater. Trans. A 48 (1) (2017) 446–458.
[84] M. Lentz, M. Klaus, I.J. Beyerlein, M. Zecevic, W. Reimers, M. Knezevic, In situ X-ray diffraction and crystal plasticity modeling of the deformation behavior of extruded Mg–Li–(Al) alloys: an uncommon tension–compression asymmetry, 0, Acta Mater. 86 (2015) 254–268, https://doi.org/10.1016/j.actamat.2014.12.003.
[85] M. Lentz, et al., Effect of age hardening on the deformation behavior of an Mg–Y–Nd alloy: in-situ X-ray diffraction and crystal plasticity modeling, 0, Mater. Sci. Eng., A 628 (2015) 396–409, https://doi.org/10.1016/j.msea.2015.01.069.
[86] A. Alankar, P. Eisenlohr, D. Raabe, A dislocation density-based crystal plasticity constitutive model for prismatic slip in α-titanium, Acta Mater. 59 (18) (2011) 7003–7009, https://doi.org/10.1016/j.actamat.2011.07.053.
[87] J. Wang, M. Zecevic, M. Knezevic, I.J. Beyerlein, Polycrystal plasticity modeling for load reversals in commercially pure titanium, Int. J. Plast. 125 (2020) 294–313, https://doi.org/10.1016/j.ijplas.2019.09.013.
[88] B.S. Fromm, B.L. Adams, S. Ahmadi, M. Knezevic, Grain size and orientation distributions: application to yielding of a-titanium [Online], Acta Mater. 57 (8) (2009) 2339–2348, http://www.sciencedirect.com/science/article/pii/S1359645409000068.
[89] D.J. Savage, Z. Feng, M. Knezevic, Identification of crystal plasticity model parameters by multi-objective optimization integrating microstructural evolution and mechanical data, Comput. Methods Appl. Mech. Eng. 379 (2021), 113747, https://doi.org/10.1016/j.cma.2021.113747.
[90] D.J. Savage, R.J. McCabe, M. Knezevic, An automated procedure built on MTEX for reconstructing deformation twin hierarchies from electron backscattered diffraction datasets of heavily twinned microstructures, Mater. Char. 171 (2021), 110808, https://doi.org/10.1016/j.matchar.2020.110808.
[91] M. Ardeljan, M. Knezevic, Explicit modeling of double twinning in AZ31 using crystal plasticity finite elements for predicting the mechanical fields for twin variant selection and fracture analyses, Acta Mater. 157 (2018) 339–354, https://doi.org/10.1016/j.actamat.2018.07.045.
[92] M. Knezevic, A. Levinson, R. Harris, R.K. Mishra, R.D. Doherty, S.R. Kalidindi, Deformation twinning in AZ31: influence on strain hardening and texture evolution [Online], Acta Mater. 58 (19) (2010) 6230–6242, http://www.sciencedirect.com/science/article/pii/S1359645410004854.
[93] M. Knezevic, M.R. Daymond, I.J. Beyerlein, Modeling discrete twin lamellae in a microstructural framework, Scripta Mater. 121 (2016) 84–88, https://doi.org/10.1016/j.scriptamat.2016.04.026.
[94] M. Jahedi, B.A. McWilliams, P. Moy, M. Knezevic, Deformation twinning in rolled WE43-T5 rare earth magnesium alloy: influence on strain hardening and texture evolution, Acta Mater. 131 (2017) 221–232, https://doi.org/10.1016/j.actamat.2017.03.075.
[95] W.G. Feather, et al., Mechanical response, twinning, and texture evolution of WE43 magnesium-rare earth alloy as a function of strain rate: experiments and multi-level crystal plasticity modeling, Int. J. Plast. 120 (2019) 180–204, https://doi.org/10.1016/j.ijplas.2019.04.019.
[96] M. Jahedi, B.A. McWilliams, F.R. Kellogg, I.J. Beyerlein, M. Knezevic, Rate and temperature dependent deformation behavior of as-cast WE43 magnesium-rare earth alloy manufactured by direct-chill casting, Mater. Sci. Eng., A 712 (2018) 50–64, https://doi.org/10.1016/j.msea.2017.11.092.
[97] A.M. Cantara, M. Zecevic, A. Eghtesad, C.M. Poulin, M. Knezevic, Predicting elastic anisotropy of dual-phase steels based on crystal mechanics and microstructure, Int. J. Mech. Sci. 151 (2019), https://doi.org/10.1016/j.ijmecsci.2018.12.021.